# **Equilibrium-Approximated Solutions to the Reactive Lauwerier Problem: Thermal Fronts as Controls on Reactive Fronts in Earth Systems**

#### Roi Roded

Civil, Environmental, and Geo-Engineering, University of Minnesota Twin Cities, Minneapolis, MN, USA

Correspondence to: R. Roded (roi.roded@mail.huji.ac.il)

#### Abstract

10

15

20

Rates of subsurface rock alteration by reactive flows are often essentially independent of kinetic rates and governed solely by solute transport to and from reactive mineral surfaces. This allows forenables a major simplification, making that makes models tractable ineven for complex kinetic systems through the widely applied local equilibrium assumption. Here, this assumption is applied to the Reactive Lauwerier Problem (RLP), which describes non-isothermal fluid injection into a confined aquifer, driving thermally induced solubility changes and reactions, leading to chemical disequilibrium. Specifically, depending on the thermal changes drive temperature-dependent solubility nature of a given mineral, the thermally induced solubility changes can leadvariations, leading to either undersaturation and dissolution or supersaturation and precipitation reactions. Using this framework, solutions for reaction rate and porosity evolution are developed and analyzed, leading to yielding a functional time-dependent criterion for their validity that incorporates time and thermal parameters. A key feature—the coalescence of thermal and reactive fronts—is then analyzed under various conditions. Finally, the used to explore their evolution over time in different settings. The applicability of the equilibrium model for important fluid-rock interaction processes is then examined and discussed and examined, including sedimentary reservoir development, evolution and mineral carbonation in peridotite, and ore deposit formation ultramafic rocks. Notably, the approach used here to extend thermal solutions for reactive processes suggests broader applicability. The findings also highlight that such thermally driven reactive fronts, particularly near equilibrium, often become essentially stationary after a relatively short period. As a result, their spatial evolution is governed solely by geological processes operating onover much longer timescales.

## 1. Introduction

1

Natural and anthropogenic systems are often complex, involving intricate interactions between various processes, which makes developing a mechanistic understanding of the system challenging. However, the disparity in timescales between these processes often allows for significant simplification, as one process typically serves as the rate-limiting step that controls the systemsystem's overall evolution. This simplification, in turn, enables the recovery of the systemsystem's mechanistic behavior. Such systems range from climate science, where atmospheric and oceanic processes interact and operate at different timescales (Vallis, 2017)(Vallis, 2017), to multi-step biochemical processes and enzyme kinetics (Cornish Bowden, 2013)(Cornish-Bowden, 2013), traffic flow analysis (Lighthill and Whitham, 1955)(Lighthill and Whitham, 1955), epidemiology and disease spread (Anderson, 1991)(Anderson, 1991), economics (Solow, 1956)(Solow, 1956) and crystal growth (Mullins and Sekerka, 1963)(Mullins and Sekerka, 1963).

Similarly, in geothermal systems, hydro-thermo-hydro-chemical (THC) processes often involve complex interactions. In particular, geochemical kinetics can be highly intricate, involving multiple species and reactions of varying orders, which are influenced by flow and transport dynamics and thermal variations (Appelo and Postma, 2004; Kolditz et al., 2016; Phillips, 2009)(Appelo and Postma, 2004; Kolditz et al., 2016; Phillips, 2009). This complexity hinders the understanding of system behaviors and their description using tractable models. However, in many cases, the rate of transport is much slower than the reaction kinetics, effectively controlling the overall reaction rate. These conditions, known as transport-controlled, occur when the transport of reactants or reaction products dictates the reaction rate (Deng et al., 2016; Roded et al., 2020; Steefel and Maher, 2009)(Deng et al., 2016; Roded et al., 2020; Steefel and Maher, 2009).

Under transport-controlled conditions, the characteristic timescale of transport,  $t_A$ , is much larger than that of the reaction,  $t_R$ , ( $t_A \Longrightarrow t_R$ ) and the system is close to chemical equilibrium (i.e., quasi-equilibrium). In such cases, the local equilibrium assumption is often invoked, and the assumption that the reaction rate depends solely on transport allowing to greatly simplify models (Andre and Rajaram, 2005; Lichtner et al., 1996; Molins and Knabner, 2019). allows one to greatly simplify models (Andre and Rajaram, 2005; Lichtner et al., 1996; Molins and Knabner, 2019). The validity of the equilibrium model assumption is determined by a large timescale ratio and the Damköhler number, Da, which, assuming a first-order surface reaction, is given by

$$60 Da = \frac{t_{\rm A}}{t_{\rm R}} = \frac{lA_{\rm S}\lambda}{u_{\rm A}} > 1, (1)$$

where l is a local characteristic length scale,  $u_A$  denotes characteristic Darcy flux [L T<sup>-1</sup>],  $A_s$  is the specific reactive area (L<sup>2</sup> to L<sup>-3</sup> of porous medium) and  $\lambda$  is the kinetic reaction rate coefficient [L T<sup>-1</sup>] (Lichtner et al., 1996; MacQuarrie and Mayer, 2005; Appendix A provides simple derivation of the condition in <u>Leq.-1</u> for the thermally driven reactive transport conditions considered in this study).

65

70

75

80

Here, in<u>In</u> this study, equilibrium model\_approximated solutions for geothermal systems are derived, building on. These build upon and extend previous work (Roded et al., 2024b), in which thermally driven reactive transport solutions were developed within the framework of the *Lauwerier solution* (Lauwerier, 1955).(Lauwerier, 1955). The Lauwerier solution provides an analytical prediction of the thermal field development resulting from the injection of hot (or cold) fluid into a thin, non-reactive, confined layer system (Lauwerier, 1955; Stauffer et al., 2014).

The thermally-driven reactive transport solutions developed by Roded et al. (2024b) integrate temperature-dependent solubility into a reactive flow formulation while incorporating the thermal field based on the Lauwerier solution. Specifically, this setting, referred to as the Reactive Lauwerier Problem (RLP), accounts for thermal variations that drive the system out of geochemical equilibrium, thereby triggering chemical reactions. These disturbances stem from shifts in mineral solubility within groundwater, where thermal fluctuations can induce conditions of either supersaturation or undersaturation. Over time, these thermally-driven reactions lead to changes in rock porosity due to the precipitation, dissolution, or replacement of solid minerals and the associated volumetric changes (Phillips, 2009; Woods, 2015).

Depending on the natural solubility of the minerals in the system, an increase in temperature can lead to either dissolution or precipitation. This occurs because mineral solubilities can either decrease with temperature (*retrograde solubility*) or increase with it (*prograde solubility*; Jamtveit and Yardley, 1996; Phillips, 2009). A notable example includes the prograde solubility of silica, which commonly precipitates in geothermal systems from the cooling of fluids (Pandey et al., 2018; Rawal and Ghassemi, 2014; Taron and Elsworth, 2009) (Pandey et al., 2018; Rawal and Ghassemi, 2014; Taron and Elsworth, 2009). In contrast,

carbonate minerals such as calcite and dolomite exhibit an inverse relationship with temperature and retrograde solubility, which is often pronounced and influenced by CO<sub>2</sub> concentration. Depending on the conditions, either rapid dissolution or rapid precipitation can occur in the case of common carbonate minerals (Andre and Rajaram, 2005; Coudrain Ribstein et al., 1998).(Andre and Rajaram, 2005; Coudrain-Ribstein et al., 1998).

Fluid recharge or injection under constrained physical and chemical conditions, as in RLP settings, is common in both natural and engineered geothermal systems and aquifers (Hidalgo et al., 2012; Phillips, 2009; Stauffer et al., 2014). These include mineral carbonation in ultramafic rocks (Kelemen et al., 2019; Roded and Dalton, 2024) and ore deposit formation by hydrothermal flows (Ingebritsen & Appold, 2012), aquifer thermal storage, pumping or reinjection of geothermal water, and groundwater storage and recovery applications (Diaz et al., 2016; Fleuchaus et al., 2018; Maliva, 2019). (Phillips, 2009; Stauffer et al., 2014). These include aquifer thermal storage, pumping or reinjection of geothermal water, and groundwater storage and recovery applications (Diaz et al., 2016; Fleuchaus et al., 2018; Maliva, 2019), as well as implications for mineral carbonation in mafic or ultramafic rocks (Kelemen et al., 2019; Roded and Dalton, 2024).

In this study, what follows, the settings and equations are first described, which then serve to derive the equilibrium-approximated solutions for the RLP are first derived for both radial and planar flows. Next, these These solutions are then compared to the reference solutions from Roded et al. (2024b) to validate them and discuss their limitations, along with the derivation of specific criteria for the RLP setup. Then Next, the evolution of reactive fronts under quasi-equilibrium conditions is analyzed for in different scenarios settings. Interestingly, it is shown that under certain conditions, thermally driven reactive fronts cease to expand and become essentially stationary after a short timescale, remaining controlled by longer-term tectonic processes. This phenomenon is discussed in The applicability of the context of equilibrium model to key relevant processes, including these dimentary aquifer alteration of sedimentary aquifers, and natural mineral carbonation, and the formation of ore deposits.—is discussed along with an outlook for further theoretical developments.

#### 2. Settings and the Equilibrium Model Equations

90

95

100

105

110

115

This section describes the RLP under the equilibrium assumption and then outlines the specific settings and relevant governing equations. These equations provide the THC equilibrium model

(Phillips, 2009; Wood and Hewett, 1982) used to drive the solutions in this work. A comprehensive review of the more general RLP framework and its main assumptions is provided in Roded et al. (2024b) and further revised in Appendix A of this work.

#### 2.1. The **Equilibrium** Reactive Lauwerier Scenario

120

125

130

135

140

The Lauwerier problem describes the injection of a hot or cold fluid into a confined aquifer bounded by impermeable bedrock and caprock (Lauwerier, 1955; Stauffer et al., 2014). (Lauwerier, 1955; Stauffer et al., 2014). The fluid flows horizontally along the  $\zeta$  coordinate, which can represent either the radial distance (r) in an axisymmetric configuration or the Cartesian coordinate (x); in planar configuration, i.e.,  $\zeta = r$  or x. These represent the two primary geometric settings considered in this study. A schematic representation of this system is provided in Fig. 1, with the nomenclature summarized in Appendix  $\frac{DE}{D}$ .

Along the flow path downstream from the injection well, heat is transferred between the aquifer and the confining aquiclude layers, which conduct the heat. Within the aquifer, thermal variations influence mineral solubility (i.e., saturation concentration,  $c_s(T)$ ). These solubility changes, in turn, lead to undersaturation and dissolution reactions or, conversely, to supersaturation and precipitation reactions, which modify the aquifer porosity ( $\theta$ ). Whether the porosity decreases or increases, and the magnitude of thesePorosity changes, depends whether increases or decreases, depend on both the temperature difference between the injected fluid and ambient conditions, thermal changes (heating or cooling) and the solubility characteristics nature of the minerals involved (i.e., (prograde or retrograde behavior). As mentioned in the Introduction, this work further examines conditions where reaction kinetics are fast and the Damköhler number is large (Da > 1).

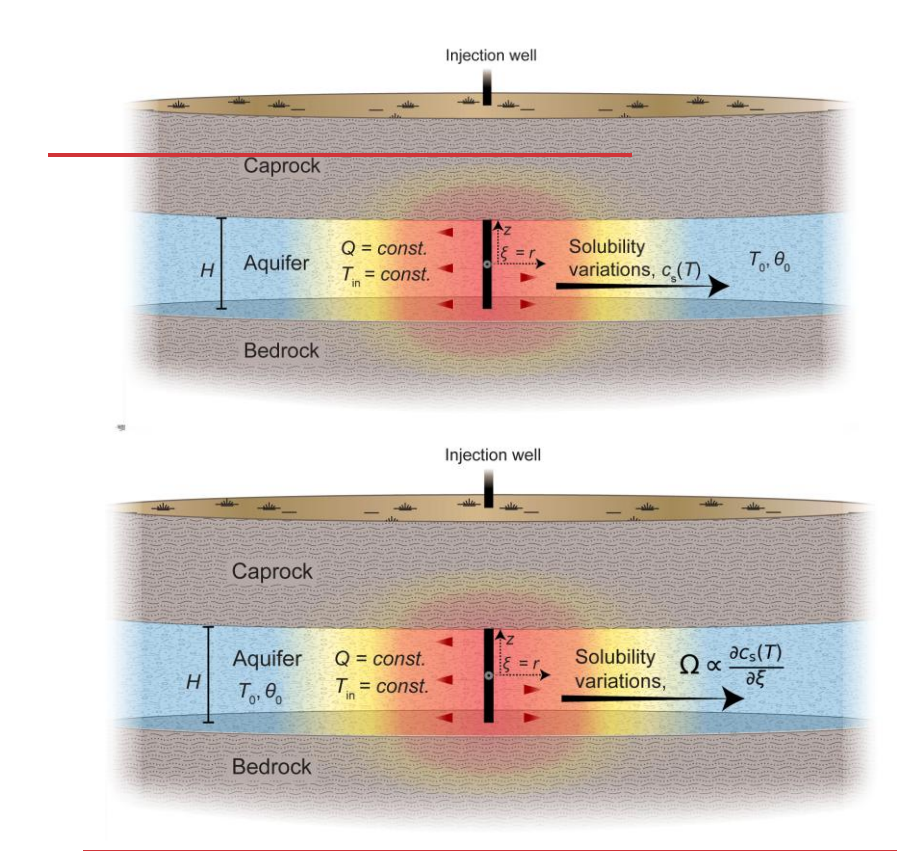


**Figure 1.** Outline of the Reactive Lauwerier Problem (RLP) for thermally driven reactive transport in geothermal systems under the equilibrium assumption. Hot (or cold) fluid is injected into an aquifer, confined between impermeable bedrock and caprock, at a steady flow rate, Q, and temperature,  $T_{\rm in}$ . The initial temperature is  $T_{\rm 0}$  and the aquifer thickness is H. Along the flow path downstream, heat from the aquifer conducts through the confining layers. The resulting thermal variations (depicted by color gradients) alter mineral solubility,  $c_s(T)$ , driving the system out of equilibrium and triggering—chemical reactions that modify the aquifer porosity from its initial value,  $\theta_0$ . In this work, it is further assumed that the High Damköhler number is large (Da > 1) conditions and that the equilibrium assumption holds. The vertical coordinate is denoted by z, whileare considered. Under these conditions, the reaction rate,  $\Omega$ , is directly governed by variations in mineral solubility,  $\partial c_s(T)/\partial \xi$ , where  $\xi$  denotes the horizontal coordinate,  $\xi$ , represents—either the radial coordinate,  $\xi$ , or the Cartesian coordinate,  $\xi$  and  $\xi$  is located at the center of the injection well, which exhibits axial symmetry (as shown in the sketch) or planar symmetry when in the Cartesian geometry is assumed case (modified after Roded et al. (2024b)).

In terms of geometry, the model considers two primary settings. The first is radial flow, which represents injection from a single well, or accounts for naturally focused flow of deep origin through faulted or fractured rock, discharging into a shallower aquifer (Craw, 2000; Micklethwaite and Cox, 2006; Roded et al., 2013, 2023; Tripp and Vearncombe, 2004). The second is planar flow, which describes injection from a row of wells arranged in a straight line configuration, as initially formulated by Lauwerier (1955).

165

170

175

180

160

#### 2.2. Main Model Assumptions

The RLP conceptual model of Fig. 1 is formulated using conservation equations for heat and reactive transport supplemented by initial and boundary conditions. The original thermal Lauwerier solution and the reactive Lauwerier solutions involve several simplifying assumptions. Here, the main ones are repeated below. For a more comprehensive overview of the assumptions, the reader is referred to Roded et al. (2024b).

Thermal assumptions include neglecting the initial geothermal gradient and assuming that the basal geothermal heat flow is small compared to the heat supplied by the injected fluid. In this study, the focus is on conditions where reaction kinetics are fast, the Damköhler number is large (Da > 1), and the local equilibrium assumption holds. Under these conditions, the reaction rate,  $\Omega$ , as shown in the next section, can be directly calculated from the thermally driven solubility changes in the system; that is,  $\Omega \propto \partial c_s(T)/\partial \xi$ . Hence, such a solution is independent of the specific reaction kinetics involved.

In terms of geometry and hydrogeological scenarios, the radial setting pertains to injection from a single well or accounts for naturally focused flow of deep-origin fluids through faulted or fractured rock, discharging into a shallower aquifer (Craw, 2000; Micklethwaite and Cox, 2006; Roded et al., 2013, 2023; Tripp and Vearncombe, 2004). The planar setting describes injection from a row of wells arranged in a straight-line configuration, as initially formulated by Lauwerier (1955).

#### 2.2. The Equilibrium-Based Approach

The steady-state, solute advection–reaction equation in the aguifer is:

190

195

200

205

210

$$0 = -u\frac{\partial c}{\partial \xi} - \Omega(\xi, t), \tag{2}$$

where  $\xi$  is the horizontal coordinate ( $\xi = r$  or x), u is the Darcy flux, c is the solute concentration and  $\Omega(\xi, t)$  is the reaction rate, which varies in space and time, t-The aquifer is also assumed to be situated at depth, preventing heat from being transferred to the surface; otherwise, there would be greater heat exchange between the aquifer and the caprock. This assumption also depends on the timescale of interest: the thermal front, which rises over time, may not extend to the surface on a short timescale. However, over a longer period, it may transfer heat to the surface, which can be calculated using the characteristic timescale of conduction  $t_C$  ( $t_C = t_C^2/c_0$ , where  $t_C$  accounts for the characteristic length scales of conduction and  $c_0$  is the thermal diffusivity).

In the confining layers, heat is transferred solely through conduction in the vertical direction ( $\varepsilon$ ), while neglecting lateral ( $\xi$ ) heat conduction. This assumption restricts the model applicability to eases with high injected fluid fluxes, where mild lateral temperature gradients evolve. To evaluate the validity of this assumption, a thermal Péclet number is employed, which compares heat advection in the aquifer to lateral heat conduction in the confirming layers:  $Pe_T = u_A l/a_b$ , where l is a length scale at which substantial temperature variation occurs (e.g., larger than 2 % from the total temperature change,  $\Delta T$ ). A posteriori inspection confirms that  $Pe_T \gg 1$  at all times at the conditions considered here. Moreover, after the initial moments, the length scale l should exceed the vertical dimension of the aquifer, l, where complete thermal mixing is assumed ( $l \gg ll$ ). This assumption may not hold if a thick aquifer (i.e., large l) is considered, and significant vertical temperature gradients are expected to develop.

Additionally, thermal and solute dispersions within the aquifer are neglected, as both thermal ( $Pe_{\rm P}$ ) and solute ( $Pe_{\rm s}$ ) Péclet numbers are assumed to be large. Properties of the fluid and solid phases, such as density and thermal conductivity, are assumed to be constant and temperature-independent. Last, it is assumed that  $Da \ge 1$  and the equilibrium assumption is applied. As a result, reaction rates are independent of kinetics ( $\lambda$ ) and the reactive surface area ( $A_{\rm s}$ ).

### 2.3. The Basic Conservation Equations

Here, the basic conservation equations are presented, simplified using the assumptions considered, and then used to develop equilibrium solutions. For a more comprehensive overview, more general versions of the conservation equations are provided in the Supplementary Material (SM). In what follows, the radial case  $(\xi = r)$  is considered first, followed by planar flow case and Cartesian coordinates  $(\xi = x)$ .

215

225

230

235

Assuming that heat transfer in the radial direction, r, is negligible, the heat equation in the bedrock and caprock confining the aquifer is,

$$\frac{\partial T}{\partial t} - \alpha_0 \frac{\partial^2 T}{\partial z^2} \quad \text{for} \quad \begin{pmatrix} \frac{H}{z \leq \frac{H}{2}} \\ \frac{H}{z \leq \frac{H}{2}} \end{pmatrix}$$

$$(2)$$

where *T* denotes temperature, *t* is time, *z* is the vertical coordinate originating at the center of the injection well and *H* denotes the aquifer thickness (see Fig. 1). The thermal diffusivity is given by 

α<sub>b</sub> = K<sub>b</sub>/Cp<sub>b</sub>, where the subscript b denotes bulk rock, *K* is the thermal conductivity, and *C*p is the volumetric heat capacity (Chen and Reddell, 1983; Stauffer et al., 2014).

Assuming that heat transport in the aquifer is dominated by advection and that perfect mixing prevails in the transverse direction (s), a 'depth averaged' heat transport equation can be derived for the aquifer domain:

$$C_{\overline{p_0}H} \frac{\partial T}{\partial t} = C_{\overline{p_1}H} \frac{1}{x} \frac{\partial (ruT)}{\partial x} \quad n \cdot \Theta(r,t), \quad \text{for} \quad \frac{H}{2} \leq z \leq \frac{H}{2}, \tag{3}$$

where subscript f denotes fluid and u(r) is the Darey flux, assumed to be uniform along the z direction and can be calculated from the total volumetric flow rate, Q, using  $u = Q/(H2\pi r)$  (Andre and Rajaram, 2005; Lauwerier, 1955). The  $\Theta$  function accounts for the heat exchange between the aquifer and the confining bedrock and caprock, calculated using Fourier's law, assuming continuous temperature at the interfaces:

$$\mathbf{Q} = -2K_{\mathbf{B}} \frac{\partial T}{\partial z}\Big|_{z=\frac{H}{2} \cdot \frac{H}{2}} \tag{4}$$

The factor of two accounts for both the bedrock and caprock (Stauffer et al., 2014). In Eq. 3, n represents a unit vector directed outward from the aquifer and perpendicular to the interface

between the aquifer and the bedrock or caprock. This orientation ensures that, e.g., in the case of a warmer aquifer, the upward and downward heat fluxes are negative.

The solute advection-reaction equation in the aquifer is:

$$0 = -u \frac{\partial \epsilon}{\partial x} - \Omega(r, t), \quad \text{for} \quad -\frac{\#}{2} \le z \le \frac{\#}{2}$$

240 (Chaudhuri et al., 2013; Szymczak and Ladd, 2012). In Eq. 2, transient variations are neglected, and the quasi-static approach to reactive flow is applied (see Appendix A and Roded et al. (2024b)).

Defining the solute disequilibrium,  $\Lambda$ , as the difference between the dissolved ion concentration, c, and the temperature-dependent solubility (i.e., saturation concentration),  $c_s(T)$ ,

$$(3)$$

where c is the solute concentration [M L<sup>3</sup>] and  $\Omega$  is the reaction rate (Chaudhuri et al., 2013; Szymezak and Ladd, 2012)2 can then be rewritten as:

$$0 = -u \left[ \frac{\partial \Lambda}{\partial \xi} + \frac{\partial c_{s}}{\partial \xi} \right] - \Omega(\xi, t). \tag{4}$$

- Next, conditions of a high Da number are considered, where reaction rates significantly exceed the rate of advective transport. In this regime, local quasi-equilibrium is maintained along flow paths, and the solute disequilibrium magnitude remains small compared to the overall solubility variation.

  Specifically,  $\Lambda \ll \Delta c_s$ , where  $\Delta c_s$  denotes the absolute solubility change in the system,  $\Delta c_s = |c_s(T_{in})| c_s(T_0)|$ , that is, between solubility at the injection temperature,  $T_{in}$ , and at ambient conditions,  $T_0$ .
- 255 Under this assumption, the first advective term in Eq. 4 (u∂Λ/∂ξ) becomes negligible compared to the other terms. The governing equation can thus be approximated as (Andre and Rajaram, 2005; Phillips, 2009, p. 237):

$$\Omega(\xi, t) = -u \frac{\partial c_{s}(T)}{\partial \xi}.$$
 (5)

The expression in Eq. 5 provides the THC equilibrium model and demonstrates that, under quasiequilibrium conditions, the solute concentration, c, closely follows the spatially varying solubility determined by the temperature field,  $c_s(T)$ . Notably, it shows that in this regime, the solution for the overall reaction rate,  $\Omega(\xi, t)$ , can be independent of the specific reaction kinetics involved and can be calculated from the solubility gradient.

260

265

270

280

Lastly, it is noted that the current study focuses on the equilibrium assumption and solves the reduced form given in Eq. 5. This contrasts with the preceding work (Roded et al., 2024b), which focused on solving the full form of Eq. 2 (or Eq. 4) under the assumption of first-order kinetics.

Note that the transient and dispersivity terms in Eq. 5 are neglected, with the latter being omitted due to the assumption of  $Pe_s >> 1$  (see SM). The justification for neglecting the transient term and invoking the quasi static approximation in the derivation of Eq. 5, lies in the separation of timescales between the relaxation of solute concentration ( $t_A$ ), heat conduction ( $t_C$ ) in the confining rocks and mineral alteration (for in depth analysis and discussion see Roded et al. (2024b) and as well, e.g., Bekri et al., 1995; Ladd and Szymczak, 2017; Lichtner, 1991; Roded et al., 2020).

Assuming a surface controlled reaction and first-order kinetics, the reaction rate can be calculated using:

$$\Omega = A_{\nu} \lambda \lambda_{\nu} \tag{6}$$

where  $A_s$  is the specific reactive surface area (L<sup>-1</sup>) and  $\lambda$  is the kinetic rate coefficient [L T<sup>-1</sup>] (Dreybrodt et al., 2005; Steefel and Maher, 2009). A is defined here as the solute disequilibrium, comprising the difference between the concentration of dissolved ions and the saturation (equilibrium) concentration,  $c_s$ ,

$$A = c - c_0(T). \tag{7}$$

Thus, the solute disequilibrium,  $\Lambda$ , is positive for supersaturation and negative for undersaturation.  $c_s$  is calculated as:

$$c_{\kappa}(T) = c_{\kappa}(T_{\mathrm{H}}) + \beta(T - T_{\mathrm{H}}),\tag{8}$$

where  $T_0$  denotes the initial temperature in the aquifer and the parameter  $\beta = \partial c / \partial T$ . In Eq. 8, a linear relation between  $c_s$  and T is assumed, with a constant proportionality factor  $\beta$ , which is positive for minerals of prograde solubility and negative for minerals of retrograde solubility (Corson and Pritchard, 2017; Woods, 2015).

Using the reaction rate from Eq. 6, the change in porosity,  $\theta$ , can be calculated as:

$$\frac{\partial \theta}{\partial t} = \frac{\Omega}{v_{\text{cons}}}, \text{ for } \frac{H}{2} \le z \le \frac{H}{2}.$$
 (9)

Here,  $c_{\text{sol}}$  represents the concentration of soluble solid mineral and v accounts for the steichiometry of the reaction. For planar flow and Cartesian coordinates, r can be substituted with x in the equations above, and Eq. 3 then takes the following form:

$$\frac{C_{p_{\overline{p}}}H}{\frac{\partial T}{\partial t}} - uC_{p_{\overline{p}}}H\frac{\partial T}{\partial x} - n \cdot \Theta(x, t), \quad \text{for} \quad -\frac{H}{2} \le z \le \frac{H}{2}. \tag{10}$$

## 2.4.2.3. Initial and Boundary Conditions

285

290

300

305

The thermal Lauwerier solution incorporates an initial conditions involve acondition of uniform temperature,  $T_{05}$ ,  $T_{0}$  across the system. The, along with boundary conditions at the injection well ( $\xi = 0$ )that specify a constant rate of fluid injection rate at temperature  $T_{10}$ , with an initial solute disequilibrium of A = 0 (Eq.  $7T_{10}$  at the injection point ( $\xi = 0$ ). It is assumed that the thickness of the bedrock and caprock, as well as the extent of the aquifer, are infinite.

With respect to the solute transport boundary conditions, the RLP problem is defined by a constant fluid injection rate at temperature  $T_{\rm in}$ , with an initial solute disequilibrium of  $\Lambda=0$  (i.e., saturated fluid) at the inlet (Roded et al., 2024b). In contrast, the equilibrium-approximated solutions derived from Eq. 5, calculate the reaction rate based on the assumption that it is proportional to the temperature-driven solubility gradient. Consequently, as will be shown in the next section, solute transport boundary conditions are not incorporated. This discrepancy is the focus of the analyses in Section 3.3.

## 3. Results: The Equilibrium Solutions and Their Applicability

#### 3.1. Derivation of the Equilibrium Solutions

#### 3.1.1. Axisymmetric (Radial) Flow

315

320

325

330

Aquifer temperature. The solution for the temperature distribution in the aquifer (known as the Lauwerier solution) derived from solving Eqs. 2 and 3 for axisymmetry is given by:

The Lauwerier solutions for the temperature distribution in the aquifer (Lauwerier, 1955; Stauffer et al., 2014) serve as the basis for developing the equilibrium-approximated RLP solutions presented here. These solutions are derived by solving the advective heat transport equation in the aquifer, together with the corresponding conductive heat transfer equation in the confining bedrock and caprock (Eqs. A1–A3 in Appendix A). The solution for axisymmetric settings is given by:

$$T(r,t) = T_0 + \Delta T \operatorname{erfc}[\zeta(r,t)r^2], \tag{11 (6)}$$

where erfc is the complementary error function,  $\Delta T = T_{\rm in} - T_0$  is the difference between injection and ambient aquifer temperatures, and  $\zeta$  is defined as:

$$\zeta(r,t) = \frac{\pi \sqrt{K_{\rm B}C_{\rm Pb}}}{QC_{\rm Pt}\sqrt{t^{\perp}}}.$$
(12)

$$\zeta(r,t) = \frac{\pi \sqrt{K_{\rm b}C_{\rm p_b}}}{QC_{\rm p_f}\sqrt{t'}},\tag{7}$$

where Q is the total volumetric flow rate, K is the thermal conductivity, and Cp is the volumetric heat capacity, with the subscripts b and f denoting bulk rock and fluid, respectively. The time variable is defined as  $t' = t - \frac{2rCp\omega(Cp_H)}{(Cp_H)}$ , and the  $t_{Lg}$ , where  $t_{Lg} = \pi r^2 HCp_{b}/(Cp_f Q)$ , with H denoting the aquifer thickness (see Fig. 1). Assuming uniform flow along the vertical direction (z), the fluid velocity can be calculated from the volumetric flow rate using  $u = Q/(H2\pi r)$ .

The solution of Eq. 116 is valid when t' > 0 (Stauffer et al., 2014). Furthermore, (Stauffer et al., 2014), and it is further assumed here that a sufficiently long time has passed and such that conditions satisfy  $t' \approx t$ . Specifically, the term  $t_{Lg}$  represents a thermal retardation time. It accounts for the delay in the arrival of the thermal front due to advective transport and the thermal energy

<u>required to heat the aquifer solid matrix along the flow path</u> (for an analysis of the validity of this assumption, see <u>Roded et al. (2024b)Roded et al. (2024b)</u>).

Additionally, for simplicity, it is assumed that the heat capacities of both the confining rocks and the aquifer are identical. To account for non-uniform heat capacities, an alternative definition of Eq. <u>416</u> can be applied (see Eqs. 3.122 and 3.131, along with the corresponding definitions in Stauffer et al. (2014)Stauffer et al. (2014)D.

#### **Thermally Driven Solubility Changes**

335

345

350

The THC equilibrium model in Eq. 5 shows that the reaction rate,  $\Omega(r, t)$ , depends on the thermally driven solubility gradient,  $\partial c_s(T)/\partial r$ . Here, the temperature-dependent solubility is calculated using:

$$c_{\rm s}(T) = c_{\rm s}(T_0) + \beta(T - T_0),$$
 (8)

Reactive solute transport. Rewriting Eq. 5 for the aquifer domain using the definition of Eq. 7 results in.

$$0 = -u \left[ \frac{\partial A}{\partial r} + \frac{\partial c_{\overline{z}}}{\partial r} \right] - \Omega(r, t). \tag{13}$$

Assuming instantaneous reaction and that quasi-equilibrium prevails,  $\Lambda \approx 0$ , so that Eq. 13 becomes,

$$\Omega = u \frac{\partial c_s(T)}{\partial x}.$$
 (14)

The where the parameter  $\beta = \partial c_s/\partial T$ . In Eq. 8, a linear relation between  $c_s$  and T is assumed, with a constant proportionality factor  $\beta$ , which is positive for minerals of prograde solubility and negative for minerals of retrograde solubility (Corson and Pritchard, 2017; Woods, 2015).

In Eq. 5, the derivative  $\partial c_s/\partial r$  can be obtained by differentiating the relationship given in Eq. 8, viz.  $\partial c_s/\partial r = \beta \partial T$  of the solubility can be expanded to  $\partial c_s/\partial r$ ,  $= (\partial c_s/\partial T)(\partial T/\partial r)$  and by further substituting the definition  $\beta = \partial c_s/\partial T$ , it can be expressed as,

355 
$$\Omega(r,t) = -u\beta \frac{\partial T}{\partial r}.$$
 (9)

The temperature gradient  $\partial T/\partial r$  is calculated by substituting the Lauwerier solution (Eq. 446) and differentiating, which yieldsperforming differentiation, yielding:

$$\frac{\beta \partial T}{\partial r} = -4\Delta T \frac{\beta \zeta r}{\sqrt{\pi}} e^{\left(-\zeta^2 r^4\right)} \Omega(r, t)$$

$$= 4u\beta \Delta T \frac{\zeta r}{\sqrt{\pi}} e^{\left(-\zeta^2 r^4\right)}.$$
(15)

The which provides the solution for the reaction rate is thus given. The evolution of porosity,  $\theta$ , is described by:

$$\Omega(r,t) = -u4\Delta T \frac{\beta \zeta r}{\sqrt{\pi}} e^{\left(-\zeta^2 r^4\right)}. \tag{16}$$

$$\frac{\partial \theta}{\partial t} = -\frac{\Omega(r, t)}{v c_{\text{sol}}},\tag{11}$$

where  $c_{sol}$  is the concentration of soluble solid mineral and v accounts for the stoichiometry of the reaction. Substituting the solution for the reaction rate,  $\Omega$  (Eq. 4610), into Eq. 911 and integrating over time yields the solution for the porosity change:

$$\theta(r,t) = \theta_0$$

$$-4u\Delta T \frac{\beta \zeta^2 r^3 t}{vc_{sot} \sqrt{\pi} vc_{sol} \sqrt{\pi}} \Gamma\left(-\frac{1}{2}, \zeta^2 r^4\right), \tag{1712}$$

where  $\Gamma$  is the incomplete gamma function.

365

## 3.1.2. Planar Flow

For the Cartesian case, with injection occurring along a lineplane, the Lauwerier solution is:

$$T(x,t)$$
  
=  $T_0 + \Delta T \operatorname{erfc}[\omega(x,t)x],$  (1813)

375 where  $\omega$  is defined as:

$$\omega(x,t) = \frac{\sqrt{K_b C_{p_b}}}{H C_{p_e} u \sqrt{t'}}, \tag{1914}$$

and  $t' = t - t_{Lg}$ , where  $t_{Lg} = xC_{pb}/(C_{piu})$ . Similarly to the radial case, the solution applies at it is assumed here that a sufficiently long times, where time has passed such that the condition  $t' \approx t$ -applies.

Following steps analogous to those in the radial case, the solutions are derived as:

$$\Omega(x,t) = \frac{1}{2u\Delta T} \frac{\beta\omega}{\sqrt{\pi}} e^{(-\omega^2 x^2)},$$
(20) (15)

and

380

390

395

385 
$$\theta(x,t) = \theta_0$$

$$-2u\Delta T \frac{\beta\omega^2xt}{vc_{sot}\sqrt{\pi}} \frac{\beta\omega^2xt}{vc_{sol}\sqrt{\pi}} \Gamma\left(-\frac{1}{2},\omega^2x^2\right). \tag{2116}$$

3.2. Applicability of the Equilibrium Approximation

3.2.1.3.2. -Comparison to the Reference Solution Solutions (High-Da)

In this section, the results of the equilibrium model solution for porosity solutions are compared with the more general solutions to the RLP model, which will henceforth be referred to as the 'reference solutions.' These reference solutions account for far-from-equilibrium conditions and assume surface-controlled reactions and first-order kinetics. The case study considered in the comparison involves a typical common scenario: dissolution of a fractured carbonate aquifer due to the injection of CO<sub>2</sub>-rich hot water and cooling-driven calcite dissolution. First, the results presented by Roded et al. (2024b) for the reference solutions are briefly summarized to facilitate the comparison with the equilibrium solutions. The reference solutions, along with the case study considered here, are detailed in Roded et al. (2024b). The reference solution equations

are further provided in Appendix B, and the parameter values used are provided in Appendix C. The reference solution equations are also provided in Appendix B, and the parameter values used are listed in Appendix D. These values are identical to those in Roded et al. (2024b), including the radial case flow rate ( $Q = 500 \text{ m}^3 \text{ day}^{-1}$ ).

400

405

410

In Fig. 2, the results of  $CO_2$ -CO<sub>2</sub>-rich hot water injection are shown at successive times since the beginningstart of the injection are shown. These represent both engineering-relevant conditions (t = 0.2,25 yr) and longer geological timescales (t = 10 kyr and 100 kyr), associated with natural processes such as focused deep-origin flow discharging into a shallower aquifer (Craw, 2000; Roded et al., 2023; Tripp and Vearncombe, 2004). The Lauwerier solution and reference solutions are shown by continuous lines (Eqs. 116 and 1382-B3), while the equilibrium solution for the porosity evolution is indicated by circle markers in Fig. 2c (Eq. 12).

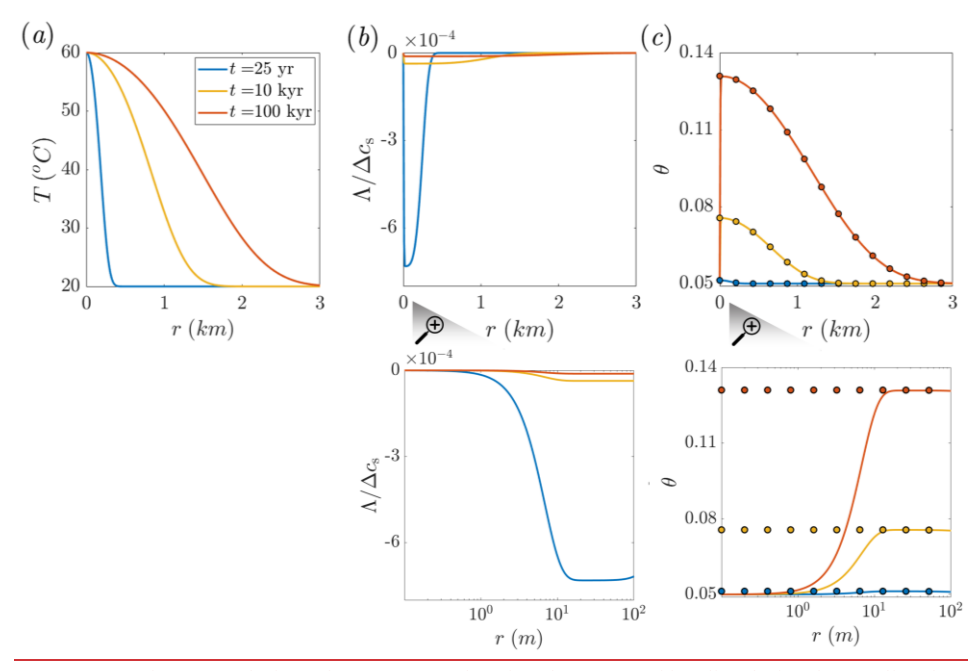


Figure 2. Reference solutions for a case study of carbonate aquifer dissolution by cooling hot water, presented for comparison with the equilibrium solution in a radial flow setting. Panels (a)—(c) show temperature (T), solute disequilibrium  $(\Lambda)$ , and porosity  $(\theta)$  plotted as functions of radial position (r) at different times. The continuous lines represent the Lauwerier solution and the

reference solutions (Eqs. 17). 6 and B2–B3), while the circles in panel (c) denote the equilibrium solution (Eq. 12). Magnified panels show solute disequilibrium ( $\Lambda$ ) and porosity ( $\theta$ ) near the inlet region.  $\Lambda$  is scaled by the total solubility variation in the system,  $\Delta c_s$ . The equilibrium solution closely matches the reference solution except near the inlet (see magnified panel and text). Quasi-equilibrium conditions are further supported by the small magnitude of  $\Lambda$ .

420

430

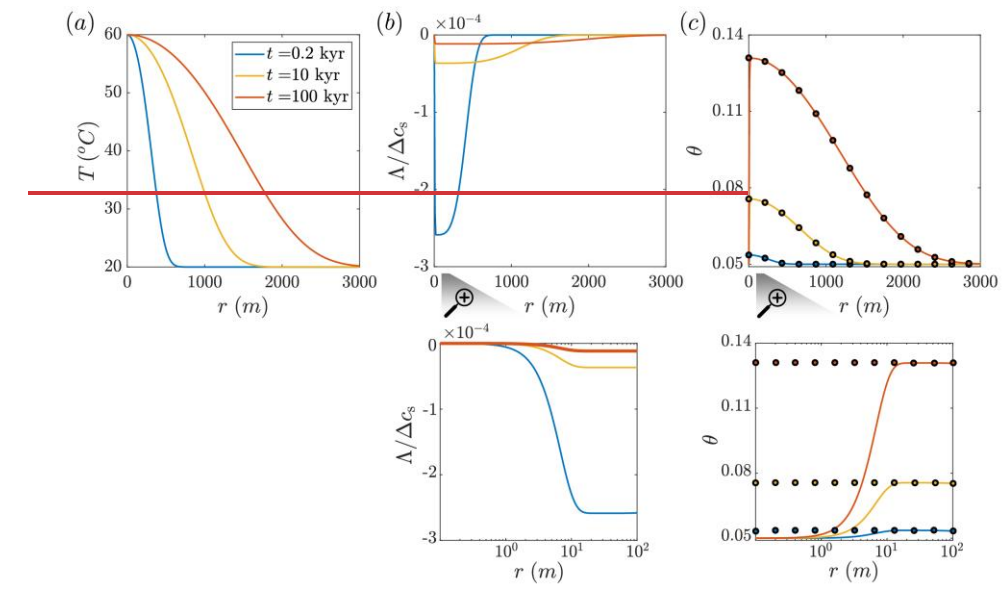
435

440

During the radial flow within the aquifer, the hot fluid cools by transferring heat into the confining layers, which heat up with time, resulting in the gradual advancement of the thermal front downstream (Fig. 2a). The cooling induces solute disequilibrium ( $\Lambda$ ) associated with undersaturation (note that  $\Lambda$  is negative for undersaturation and positive for supersaturation, see Eq. 73). The magnitude of  $|\Lambda|$  in the aquifer is small compared to the absolute solubility change in the system,  $\Delta |\Lambda|/\Delta c_s \ll 1\%$  ( $\Delta c_s = |c_s(T_{in}) - c_s(T_0)|$ , i.e., between  $c_s(T_{in})$  at the injection point to  $c_s(T_0)$  at ambient conditions ( $|\Lambda|/\Delta c_s \ll 1\%_5$ ); see Fig. 2b). The small magnitude of disequilibrium is associated with relatively high  $\frac{PCO_2CO_2}{CO_2}$  partial pressure considered (0.03 MPa) and rapid kinetics under these conditions.

Despite its small magnitude, the disequilibrium,  $\Lambda$ , governs the alteration of the aquifer and the evolution of its porosity. Notably, since the water at the inlet is hot and saturated with calcite,  $c = c_s(T_{\rm in})$ , disequilibrium and the reaction rate are zero at the inlet, resulting in no change in porosity (see Fig. 2b and  $\frac{3ec}{c}$ , along with their magnified views). Disequilibrium (undersaturation) abruptly develops downstream of the injection well, initially forming a small minimum (at  $r \approx 20$  m) before gradually diminishing to zero further downstream.

In accordance with the disequilibrium, the porosity profile sharply increases near the inlet and then gradually decreases downstream (Fig. 2c). Undersaturation and dissolution along the flow path are governed by the interplay of three processes: (I) dissolution, which reduces undersaturation (bringing  $\Lambda$  closer to zero), (II) progressive cooling, which enhances undersaturation, and (III) advection, which transports reaction products (calcium ions) radially outward from the well, sustaining undersaturation. Here, fluid velocity and advection decay with a distance, following a 1/r relationship. Particularly, the thermal changes are also reflected in the time evolution. At an early time (t = 25 yr), disequilibrium and its gradients are relatively high. As the thermal front advances and thermal gradients decrease, the disequilibrium curves flatten.



445

450

455

460

The Figure 2. Comparison between the reference solutions and the equilibrium solution for the ease study of carbonate aquifer dissolution by cooling hot water. Temperature (T) solute disequilibrium (A) and porosity  $(\theta)$  in the aquifer are plotted as functions of radial position (r) at different times. matches the reference The continuous lines represent the Lauwerier solution and the reference solutions (Eqs. 11 and B.1-3 from Appendix B), while the circles in panel (c) denote the equilibrium solution (Eq. 17). (a) The hot flow cools as it flows, the confining rocks heat up, and the thermal front advances downstream. (b) Cooling induces undersaturation (negative disequilibrium, A, see Eq. 7). A is scaled by the total solubility variation in the system,  $\Delta c_s$ , (refer to the text for the definition of  $\Delta c_s$ ). At the inlet, the water is hot and saturated, with  $c = c_s(T_{in})$ . Undersaturation sharply forms near the inlet ( $r \approx 20$  m, as shown in the magnified panel of the region near the inlet) and gradually decreases along the flow path due to dissolution reactions, with A approaching zero. As the thermal front advances downstream and the thermal gradients become milder, the A curves also flatten. (c) In accordance with the A profile, a porosity profile evolves over time. The equilibrium solution closely agrees with the reference solution, except adjacent to the inlet (see magnified panel and text). Quasi-equilibrium conditions are also evident from the small magnitude of A, which results from the relatively rapid kinetics (high Da).

The equilibrium model solution matches closely the reference solution and is violated only elosely near the inlet (r < 20 m; Fig. 2c). The agreement between the solutions and the existence of quasi-equilibrium conditions is supported by the small magnitude of the disequilibrium in the reference solution. This is because the equilibrium model assumes  $\Lambda = 0$  (cf. Eqs. (A) in the reference

solution. While the  $\underline{4}$  and 5); therefore, a small  $\Lambda$  confirms the validity of this approximation. Consequently, solute disequilibrium provides an effective metric for quantifying the spatial and temporal extent to which the equilibrium assumption holds. This will be used next to further assess the applicability of the equilibrium-approximated solutions (Section 3.3).

With respect to the discrepancy near the inlet between the solutions, the injection of hot, saturated water does not resultresults in no porosity changes atchange in the inlet reference solution. In contrast, the equilibrium model, which approximates assumes the reaction rate based depends on advective and cooling rates (Eq. 14), the temperature gradient alone, does not capture this effect. Although Particularly, the solute transport boundary condition of inlet saturation ( $\Lambda = 0$ ) is not incorporated into the equilibrium-approximated solutions, leading to this discrepancy (referred to hereafter as the 'inlet advective discrepancy').

<u>Under the conditions here</u>, the deviation between the solutions is limited to a <u>smallnarrow</u> region, it may still be significant near the inlet. However, in the ease of dissolution, assome cases, locally lowreduced porosity and permeability values can <u>impactstill influence</u> the overall estimation of aquifer permeability (Roded et al., 2024b). <u>In particular, overestimation of porosity and permeability While the deviation in these cases can be accounted for by assuming no reaction at the inlet, as will be shown in Section 3.3, this cannot capture advective effects that may become <u>significant</u> near the inlet <u>can lead to an overestimation of the aquifer effective permeability.</u> However, in other cases, this deviation may be negligible. Furthermore, under low *Da* conditions. It is also noted that in most practical scenarios, the injected fluid is expected to cool slightly as it flows down during its descent in the well, and <u>may</u> therefore, it may already be reactive upon entering the aquifer.</u>

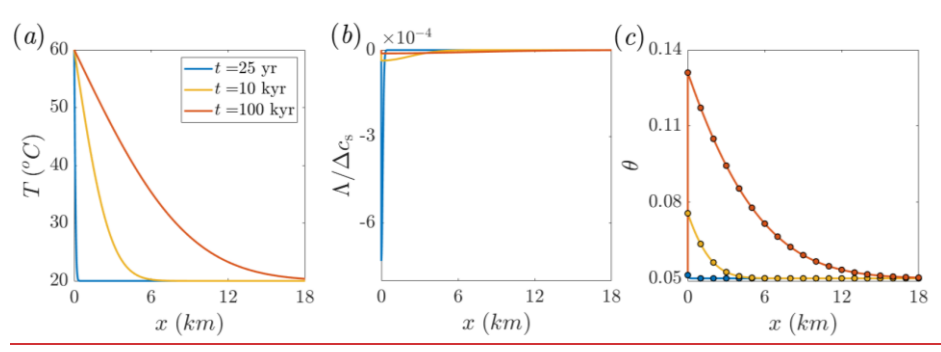


Figure 3. Reference solutions for a case study of carbonate aquifer dissolution by cooling hot water, presented for comparison with the equilibrium solution in a planar flow setting. Panels (a)–(c) show temperature (T), solute disequilibrium ( $\Lambda$ ), and porosity ( $\theta$ ) as functions of position (x) at different times. The continuous lines represent the thermal Lauwerier solution and the reference solutions (Eqs. 13 and B5–B6), while the circles in panel (c) denote the equilibrium solution (Eq. 16).  $\Lambda$  is scaled by the total solubility variation in the system,  $\Delta c_s$ . Similar to the radial case, the equilibrium solution closely matches the reference solution except near the inlet. This is also supported by the small magnitude of  $\Lambda$ .

For completeness, Fig. 3 presents results for the same case study shown in Fig. 2 under a planar flow setting, with a fluid velocity of  $u = 10^{-6}$  m s<sup>-1</sup>. Similar to the radial case, the equilibrium solution closely matches the reference solution, with deviation occurring only near the inlet (magnification not shown). A key difference from the radial case is that the aquifer is heated over significantly greater distances. This results from the uniform flow velocity and more efficient heat retention in the planar configuration. In contrast, radial flow involves velocity decay with distance, which increases residence time and enhances conductive heat loss to the surrounding rock.

Additionally, in the radial case, the heat source (e.g., an injection well) acts as a source from which hot fluid spreads outward radially. In contrast, the planar configuration can be conceptualized as injection from a distributed source (e.g., a row of wells) generating a uniform planar front. More precisely, under the perfect thermal mixing assumption, the radial case is treated mathematically as a point source, while the planar case is treated as a line source. Hence, in the radial case, heat conduction is multidirectional, whereas in the planar case, heat is conducted only in vertical directions. These differences influence the temperature profile shape. In the radial case, effective heating near the injection well and later quick decay lead to a sigmoidal (or diffusive front-like)

profile, whereas in the linear case there is a decaying profile (cf. <u>Figs. It is noted that 2</u> and 3). These differences are further quantified in Section 3.4.

With respect to the results in Figs. 2 and 3, recall that the solutions in Section 3.1 and the results shown in Fig. 2 rely on the fundamental assumption of spatial uniformity and symmetry in the reactive flow. However, in practical scenarios, dissolution channels (wormholes) may develop at the reaction front (Chadam et al., 1986; Furui et al., 2022; Roded et al., 2021). These wormholes localize reactive flow, creating heterogeneous flow fields that deviate from the assumed symmetry and uniformity. Consequently, the results in FigFigs. 2 and 3 represent only an average solution and do not capture local flow variations accurately.

Additionally Furthermore, the model was equilibrium solutions were also found to applybe applicable to the injection of hot, silica-rich water into a sandstone aquifer, where cooling leads to induces supersaturation, silica precipitation, and porosity reduction, as discussed in Roded et al. (2024b) Roded et al. (2024b) (not presented). In summary, the results in this section validate the equilibrium solutions against the reference solutions, and highlight the inlet advective discrepancy, examined next (Section 3.3). These results also demonstrate their overallbroader applicability across a broad range of characteristic conditions in natural and applied systems, as further discussed laborated in the Discussion section.

### 3.2.2. System Shift Over Time

515

520

525

530

535

This section analyzes the system state change over time and its evolution toward quasiequilibrium, as reflected by the differences in predicted reaction rates between the solutions, as functions of time. Conditions of precipitation ( $\beta \ge 0$ ) are considered with a kinetic rate coefficient nearly four orders of magnitude lower ( $\lambda = 5 \cdot 10^{-10}$  m/s), while keeping the rest of the parameters the same as in Section 3.2.1. This scenario corresponds, for example, to calcite precipitation under neutral conditions (Plummer et al., 1978).

## 3.3. Figure 3aApplicability of the RLP Equilibrium Solutions

This section further examines the applicability of equilibrium-approximated solutions, focusing on the inlet advective discrepancy. This is done by considering lower *Da*, conditions farther from equilibrium, and changes in the system state over time. Accordingly, a scenario of relatively slow

precipitation ( $\beta > 0$ ) is considered, using a kinetic rate coefficient nearly four orders of magnitude lower ( $\lambda = 5 \cdot 10^{-10}$  m/s), while all other conditions remain consistent with Section 3.2. This setup is representative, for example, of carbonate mineral precipitation from water of alkaline composition originating in carbonate or mafic rock aquifers (e.g., basaltic formations). Upon reinjection and subsequent heating, the solubility of carbonate phases decreases, promoting CO<sub>2</sub> mineralization through precipitation reactions (Etiope, 2015; Plummer et al., 1978; Steefel and Lichtner, 1998).

540

545

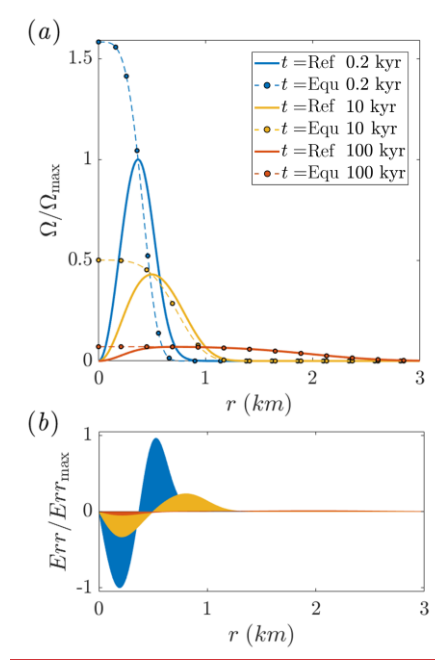


**Figure 4.** Comparison of the reference and equilibrium solutions over time under low Da conditions. (a) Reaction rate,  $\Omega$ , as a function of radial position (r) at different times. The continuous lines represent the reference solution (Eq. B3), and the circles represent the equilibrium solution (Eq. 10), denoted as 'Ref' and 'Equ' in the legend, respectively. (b) The deviation between the solutions, shown using the local error, Err, is visualized as a shaded region. Err is calculated as the radial integral of the difference between the solutions (see text for details).  $\Omega$  and Err are normalized by their maximum values at t = 0.2 kyr, where  $\Omega_{max}$  refers to the reference solution.

<u>Figure 4a</u> presents the results for the reaction rate,  $\Omega$ , for the reference solution (solid lines; <u>Eq.</u> <u>B3-Eqs. B.1 and 3</u>) and the equilibrium solution (dashed lines with circle markers; Eq. <u>1610</u>). The

lower reaction rates slower kinetics and reduced Damköhler number,  $Da_7$  result in a significantly larger disequilibrium magnitude, A, and greater deviation compared to the case presented in Fig. 2. Additionally shown in Figs. 2c and 3c. Note that the results in Figs. 2c and 3c, rather, present the porosity evolution, which reflects the time-integrated behavior of  $\Omega$  (see Eq. 11).

Significantly, the peak magnitude of disequilibrium of the reaction rate curve in Fig. 4a is attained reached further downstream, rather than occurring immediately near the inlet as observed in Figs. 2 and 3. This shift reflects a much more dominant advective effect but still preserves the same general behavior: advection of saturated fluid from the inlet and the progressive buildup of disequilibrium and elevated  $\Omega$  occur downstream of the injection well. However, in this case, the effect extends over a much greater distance.

560

565

570

575

580

Notably, Another prominent effect visible in Fig. 3a,4a is the reduction in deviation between the solutions decreases as over time progresses. This trend is also illustrated quantified in Fig. 3b4b, which shows the weighted local error, Err, calculated as from the difference between the two solutions integrated in the radial direction,  $Err = (\Omega_{Ref} - \Omega_{Equ}) \frac{2\pi r dr}{2\pi r}$ , where the subscripts Ref and Equ denote the reference and equilibrium solutions, respectively. Fig. 3b presents only the positive values of

<u>The Err as the coloredshaded</u> regions (the magnitude of the negative values being equal due to solute conservation in the solutions).

The Err curves show a progressive decrease and flattening over time. This reduction in Err and the closer approach to quasi-equilibrium are attributed to the thermal front advancing downstream-advancement of the thermal front. As the thermal front advances and extends, the temperature gradients near the inlet become milder, leading. This leads to a decrease in the reaction rate in this region. The temperature gradients also reach further downstream to regions with lower flow velocity, and higher local Da, causing the deviation between the solutions to diminish. This is illustrated by the inlet advective discrepancy of the black curve, which shows equilibrium model becomes less pronounced (the trend of 1/Da with Supplementary Material presents results for the radial distance from planar case, which exhibits the inlet same effects).

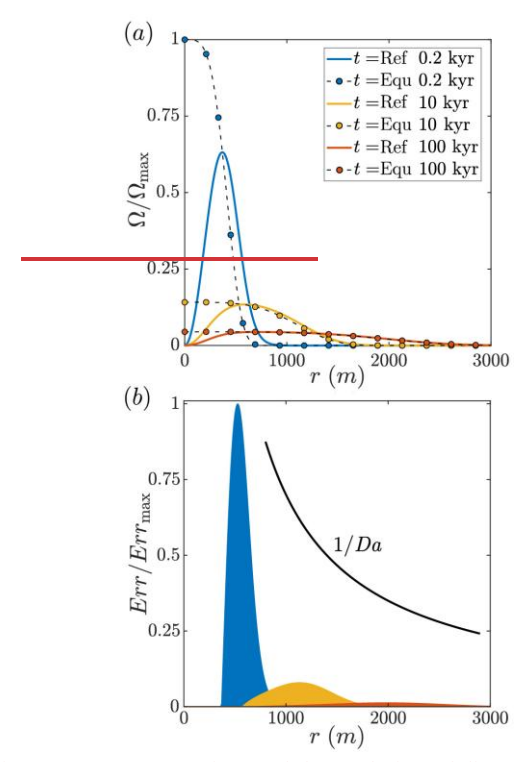


Figure 3. Shift in system state over time and the evolution of distance to equilibrium at low Da conditions. (a) Reaction rate,  $\Omega$ , for the equilibrium solution (Eq. 16) and the reference solution (Eq. B.3) as functions of radial position (r) at different times. 'Equ' and 'Ref' in the legend denote the equilibrium and reference solutions, respectively. Notably, the deviation between the solutions decreases as time progresses. (b) This is also illustrated by the plots of the error, Err, shown as colored region. Err is calculated as the radial integral of the difference between the solutions in (a) (refer to text). The Err progressively decreases and flattens over time, reflecting the system approach to quasi-equilibrium as the thermal front advances downstream. As the front stretches, temperature gradients near the inlet become milder and extend into areas with lower flow velocity and higher local Da. The trend of 1/Da with radial distance from the inlet is shown by the black curve.

#### 3.3. Equilibrium Criterion Derivation

585

590

595

As noted in the Introduction, the applicability of the equilibrium model is determined governed by the Damköhler number, Da, with quasi-equilibrium conditions prevailing expected when Da > 1 (Eq. 1). In this section, the factors promoting quasi-equilibrium in the specific settings of

the RLP are analyzed, with particular focus on the influence of thermal parameters and time. This analysis enables, the deviation associated with the equilibrium solutions, which primarily arises from the local inlet effect, evolves over time and is influenced by thermal dynamics. This observation motivated the derivation of the functional relationship between key parameters, variables, and the system equilibrium state. As more specific applicability criterion, presented in Appendix C. This analysis is based on a key feature of quasi-equilibrium isbehavior: the close alignment of the thermal and reactive fronts in the aquifer (see , which occurs when Da is high (cf. Fig. 2a and b). This feature behavior is leveraged to establish a criterion for when these fronts coincide, and equilibrium conditions can be assumed. It is important to note that even when the fronts coincide, far from and equilibrium conditions may still persist upstream. Nonetheless, the derived functional relationships offer useful guidance.

First, the thermal front end location,  $r_{\rm F}$ , is defined as the position where the temperature deviates slightly from the ambient value,  $\varepsilon = (T(r_{\rm F}) - T_0)/\Delta T$ , where  $\varepsilon << 1$ . Substituting this definition into Eq. 11 leads to

$$\varepsilon = \operatorname{erfc}(a)$$
, where  $a = \zeta(t)r_{\mu}^{2}$ . (22)

For example, for c = 0.01  $a \approx 1.8$ , be assumed. This functional relation, which applies to both planar and radial settings, is given by:

Then, re-ean be expressed as,

605

610

620

$$r_{\pm} = \sqrt{\frac{\zeta(\pm)}{\zeta(\pm)}}.$$
 (23)

Next, an approximate form of the reference solution for disequilibrium is used, assuming quasi-equilibrium and the coalescence of the thermal and reactive fronts (Eq. B.3 in Appendix B; Roded et al., 2024b). In this solution, by substituting the front-end location,  $r_{\rm F}$ , and the condition  $\varepsilon \ge \Delta/\Delta c_{\rm s}$ , we obtain:

$$\frac{\epsilon \ge \frac{\Delta T}{2} \frac{\beta}{\sqrt{\pi}} e^{\left(-\eta r^2\right)} \left( \frac{e^{\left(\eta r_E^2 - \zeta^2 r_E^4\right)}}{\frac{\eta}{2\zeta} - \zeta r_E^2} - \frac{2\zeta}{\eta} \right).$$
(24)

Substituting the definition from Eq. 23, neglecting early times, and assuming high Da and  $\eta >> \zeta$ , Eq. 24 finally becomes:

625

635

640

645

$$c \ge \frac{\Delta T}{\Delta c_{+}} \frac{\beta}{\sqrt{\pi}} \frac{2\zeta}{\eta}$$
 (25)

Noting that  $\beta = \Delta c_s/\Delta T$  and explicitly substituting the parameters using Eq. 12 and  $\eta = H\pi A_s J/Q_s$ . Eq. 25 becomes,

 $330 \gg \frac{2}{\sqrt{\pi t}} \left(\frac{1}{A_{\rm S}\lambda}\right) \left(\frac{\sqrt{K_{\rm b}C_{\rm p_b}}}{HC_{\rm p_f}}\right). \tag{2617}$ 

Equation 26 defines the conditions under which the thermal and reactive fronts coincide and provides a functional relationship to the state of equilibrium. As shown in the previous section and in Fig. 3, the criterion demonstrates In accordance with the results in Fig. 4, the criterion shows that the system approaches equilibrium as time progresses (with a proportionality of  $t^{1/2}$ ). The second term in the brackets represents the characteristic reaction timescale of the reaction,  $t_R = 1/A_s\lambda$ , which, in accordance agreement with the high Da condition, indicating indicates that when a smaller  $t_R$  is small, the system approaches leads to faster approach to equilibrium more rapidly. The final term in the brackets represents captures the ratio between of thermal parameters, showing that when the confining rock parameters of heat rock's thermal conductivity ( $K_b$ ) and heat capacity ( $C_{pb}$ ) are small low, the thermal front advances downstream more quickly rapidly, promoting equilibrium. Conversely, when the Similarly, a large product of aquifer thickness and fluid heat capacity ( $HC_{pf}$  is large, the) also facilitates faster thermal front also advances quickly downstream, facilitating advancement and equilibrium.

Notably, the volumetric flow rate (Q) fluid velocity does not appear in the criterion of Eq. 26, as 17. This is attributed to the fact that solute advection enhances disequilibrium (in accordance with the Da criterion), while thermal advection promotes equilibrium by extending and stretching the thermal front. By introducing the fluid velocity, u, and the characteristic length scale, l, into the expression, the criterion in Eq. 17 can be reformulated in terms of two functions:

This criterion of Eq. 26 can be further rewritten in terms of two functions,

650 
$$1 \gg f(r_{+})g(t, r_{+}), \tag{27}$$

$$1 \gg f^{-1}g(t),\tag{18}$$

where

670

$$f(r_{\mathbb{F}}) = \frac{lu(r_{\mathbb{F}})}{A_{\mathbb{F}}\lambda} = \frac{lA_{\mathbb{S}}\lambda}{u} \quad \text{and} \quad g(t, r_{\mathbb{F}}) = \frac{2}{\sqrt{\pi t}} \frac{\sqrt{K_{\mathbb{B}}C_{\mathbb{P}_{\mathbb{B}}}}}{lu(r_{\mathbb{F}})HC_{\mathbb{P}_{\mathbb{F}}}}(t)$$

$$= \frac{2}{\sqrt{\pi t}} \frac{l\sqrt{K_{\mathbb{B}}C_{\mathbb{P}_{\mathbb{B}}}}}{uHC_{\mathbb{P}_{\mathbb{F}}}}.$$
(19)

The first function,  $f(r_F)$  can be referred to as a dynamic Da number that changes with the position of  $r_F$ -and describes the relative effect of reaction versus advective transport versus reaction. The second function  $g(t,r_F)$ , accounts for the evolution and advancement of the thermal front without time.

The functional criterion in Eqs. 17 and 18, in accordance with the results in Fig. 4, demonstrates that the equilibrium solutions are not applicable as t → 0 and become less accurate at initial stages. However, as demonstrated in Fig. 2, the equilibrium-approximated solutions may remain fully valid even at relatively early times. This behavior is observed under common conditions involving fractures carbonate aquifers and silica precipitation, where the validity extends to timescales relevant to engineering applications (e.g., t < 25 yr).</li>

It is recalled here that several inherent assumptions in the Lauwerier solution reduce its accuracy during initial stages (see Appendix A). Moreover, the assumption taken here of negligible thermal retardation time ( $t_{Lg}$ ) and the approximation  $t' \approx t$  employed in the Lauwerier solution affect the accuracy at early times (see Eqs. 6 and 13). This assumption, which is particularly relevant for the radial case, leads to reduced accuracy at early times (e.g.,  $t \le 10$  years; see Appendix C in Roded et al. (2024b)).

## 3.4. Development of Coalesced Fronts

Equation 23, along with one that applies to the planar case, can be used to infer the coalesced thermal and reactive front extensions,  $\underline{x}_{\mathbb{R}}$  and  $r_{\mathbb{R}}$ , under quasi equilibrium conditions. These provide:

675

680

685

 $x_{+}(t)$  =As mentioned in the previous section, a key feature of quasi-equilibrium behavior is the close alignment of the thermal and reactive fronts in the aquifer, which occurs when the Da is high and reactions dominate over transport. Under these conditions, any disequilibrium induced by thermal changes diminishes rapidly and essentially does not extend downstream of the thermal front, resulting in the coalescence of the fronts. This property is leveraged to infer in a simple manner the spatial distribution and temporal advancement of the coalesced fronts using the thermal Lauwerier solutions.

First, we define the thermal fronts' outer-end positions,  $\zeta_F(t)$ , as the furthest distances of thermal perturbation due to the injection at a given time. The thermal perturbation is quantified by  $\varepsilon = (T(\zeta_F)-T_0)/\Delta T$ , where  $\varepsilon$  is a prescribed small value ( $\varepsilon \ll 1$ ); here,  $\varepsilon = 0.01$ . This threshold uniquely determines the position  $\zeta_F(t)$  at which the temperature perturbation is considered negligible.

Next, rearranging and substituting the definition of  $\varepsilon$  corresponding to the conditions at the fronts' outer-end positions into the Lauwerier solutions (Eqs. 6 and 13) yields:

$$\varepsilon = \operatorname{erfc}(a)$$
, where  $a = \begin{cases} \zeta(t)r_{F}^{2}, & \text{for } \xi = r\\ \omega(t)x_{F}, & \text{for } \xi = x \end{cases}$  (20)

Here, a is a constant determined by  $\varepsilon$ , and for  $\varepsilon = 0.01$ ,  $a \approx 1.8$ . Then, the fronts' outer-end positions can be expressed as:

$$r_{\rm F}(t) = \sqrt{\frac{a}{\zeta(t)}}, \quad \text{and} \quad x_{\rm F}(t) = \frac{a}{\omega(t)}.$$
 (21)

Finally, substituting the definitions of  $\zeta$  and  $\omega$  (Eqs. 7 and 14) into Eq. 21 gives explicit expressions for the advancement of the coalesced fronts under quasi-equilibrium conditions:

695 
$$\frac{\frac{aHC_{p_{f}}}{\sqrt{K_{B}C_{p_{B}}}} t^{\frac{4}{2}}}{\frac{1}{\sqrt{K_{B}C_{p_{B}}}}} t^{\frac{1}{4}}, \text{ and } x_{F}(t) = \sqrt{\frac{aQC_{p_{f}}}{\pi\sqrt{K_{b}C_{p_{b}}}}} t^{\frac{1}{4}}, \text{ and } x_{F}(t)$$

$$= \frac{aHC_{p_{f}}u}{\sqrt{K_{b}C_{p_{b}}}} t^{\frac{1}{2}}. \tag{29}. \tag{22}$$

$$(a) \qquad (b) \qquad (c) \qquad (c) \qquad (c) \qquad (d) \qquad (d) \qquad (d) \qquad (d) \qquad (e) \qquad (e)$$

These relations provide a simple way to estimate the spatial positions of the coalesced fronts as a function of time using the thermal solutions alone.

To demonstrate the fronts' advancement, Eqs. 22 are used to plot  $x_F$  and  $r_F$  for three different velocities (u) and flow rates (Q), presented in Fig. 5a and b. This illustrates the decay of the advancement rate over time in both cases: the hot fluid heats the confining rocks as it flows, and the thermal fronts gradually advance downstream. However, due to continuous heat transfer to the confining layers along the flow path, the advancement rate decreases over time and distance.

700

705

710

The key difference between the radial and planar cases, as noted in Section 3.2, is clearly reflected in Eqs. 22 and the results shown in Fig. 5a and b. The planar case exhibits significantly greater heat retention and a higher advancement rate. This is demonstrated by the green dashed lines in Fig. 5a and b, which indicate that half of the final calculated extent,  $1/2x_{\text{Final}}$ , is reached in one quarter of the final time, while in the radial case,  $1/2r_{\text{Final}}$  is approached after one sixteenth of the time. Alternatively, this can be shown by differentiating Eqs. 22 with respect to time, yielding  $\partial r_F/\partial t \propto f^{3/4}$  in the radial case, compared to  $\partial x_F/\partial t \propto f^{3/2}$  in the planar case.

Another case considered here, shown in Fig. 5c and d, is the low-flow-rate limit in radial geometry, where conduction dominates and effectively distributes heat. This is illustrated using two different

approaches: (I) the analytical conduction-only solution, representing the limit  $Q \to 0$  (black lines), and (II) numerical results for low flow rates (Q = 1 and 5 m<sup>3</sup>/day, red and orange curves).

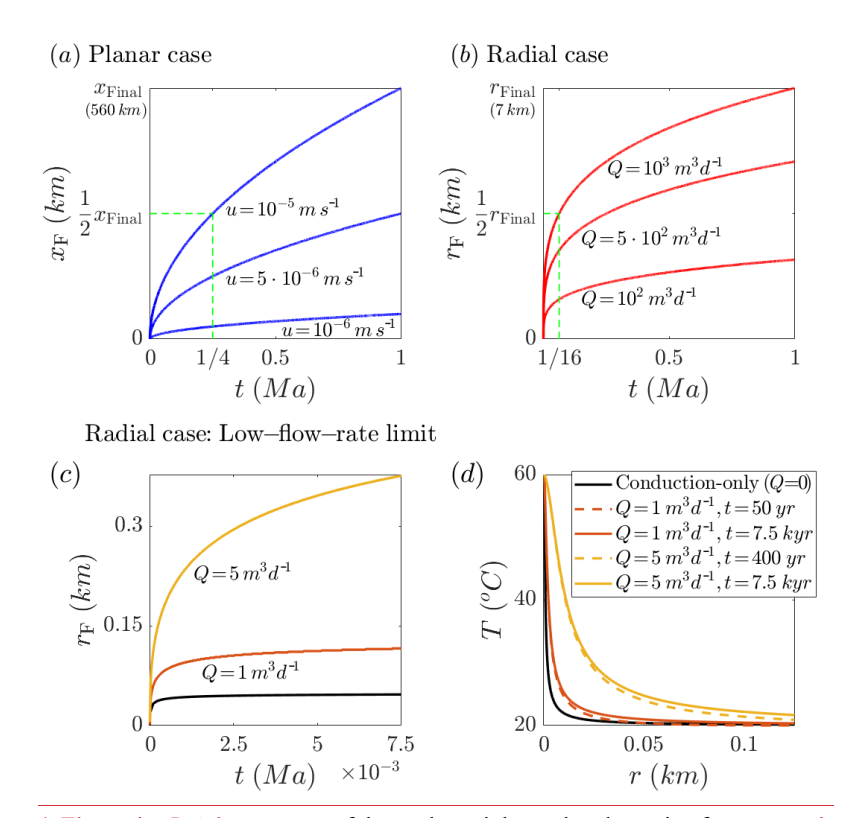


Figure 4. Elongation 5. Advancement of the coalesced thermal and reactive fronts over time,  $x_F(t)$  and  $r_F$ , over time(t), for different velocities,  $(u_7)$  and flow rates,  $(Q_7)$ , respectively. Panels  $(a_7)$  (b), and the low-) show results for high flow-rate limit assuming conduction only rates, while panels (c). (a, b) The fronts elongation over time is proportional to  $t^{1/2}$  and  $t^1$ )—(d) illustrate the low-flow-rate limit. (a)—(b)  $x_F$  and  $r_F$  are calculated using Eqs. 22. Green dashed lines illustrate the difference between the radial and planar cases: half of the final extents  $(1/2x_{Final})$  are reached at 1/4 and 1/16 of the final time, respectively, (Eq. 29), and hence the rate of elongation decreases substantially faster for the radial case and at lower flow rates. To illustrate this, half of the final calculated extension,  $1/2x_F$  is marked and shown to be reached in 1/4 of the time, while in the radial case,  $1/2R_F$  is approached after 1/16 of the time (see dashed lines). (c) The low-flow-rate limit is shown using the—)—(d) The low-flow-rate limit refers to the radial case where conduction effectively distributes heat. This is analyzed using solution for conduction-only, representing the limit  $O \rightarrow 0$  (analytical, black lines), and results for low flow rates of O = 1 and

 $5 \text{ m}^3$ /day (numerical, red and orange, respectively). Panel (c) shows  $r_F$  for these cases, while (d) displays the temperature profiles as a function of radial position, r. The black line in (d) represents the conduction-only quasi-steady-state profile, and the colored dashed and continues lines indicate early and later times, respectively, for each flow rate. The close alignment of the lines demonstrates that the thermal field is essentially stationary already at early times. For further details on the calculations, refer to the text.

The analytical solution for conduction from describes a point sourcesphere at constant temperature in an infinite space. The inner inset and the orange curve display the temperature profile, medium, modeling heat conducted from the sphere into the surrounding medium. This time-dependent solution converges to a quasi-steady-state temperature profile that remains essentially unchanged over time (Stauffer et al., 2014; see details in the SM). The numerical simulations for low flow rates use equations and settings identical to those of the Lauwerier solution but with the dashed line showing that an important distinction: they do not assume negligible radial conduction. This simplification makes the Lauwerier solution inadequate under conditions of low flow rates and sharp lateral geothermal gradients (see Appendix A). Further details of the numerical calculations are given in Roded et al. (2023).

740

745

750

755

760

Figure 5c shows  $r_F$  for the conduction-only case and for Q = 1 and 5 m³/day (other parameter values are consistent with Appendix D). Unlike the high-flow-rate planar and radial cases in Fig. 5a and b,  $r_F$  and the advancement rate essentially level off under these conditions. In particular,  $r_F$  increases with Q but also levels off over time, showing similar behavior to the conduction-only case. This is more clearly shown in Fig. 5d that shows temperature profiles for these cases as a function of radial position, r. It includes the analytical quasi-steady-state temperature profile (conduction-only case) and numerical profiles at low flow rates shown for two consecutive times, with dashed and continues lines indicating early and later times, respectively. The close alignment of the dashed (early time) and continues (later time) lines, and their almost overlap, demonstrate that the temperature profiles change very little after early times. The profiles become nearly stationary over tens to hundreds of years, which is a very brief geological timescale.

The results show effective heat distribution by conduction, with nearly complete cooling occurs of within 10 m. In this case, the front becomes quasi-stationary on a timescale of tens of years. This scenario 100 m, depending on the flow rate. Overall, both the analytical solution for the limit  $Q \rightarrow 0$  and the numerical solutions at low flow rates demonstrate similar heat

transport behavior under these conditions. This scenario of low flow rates is particularly relevant underto natural conditions, demonstrating that the which often involve low flow rates and can manifest on the surface as low-flow-rate thermal springs (Garven, 1995; Klimchouk et al., 2017; Roded et al., 2013).

These findings have important implications, suggesting that thermally driven reactive front may fronts can also become essentially nearly stationary (see , as will be further discussed in the Discussion section). Parameter values used are as in Section 3.2.1. Lastly, it is important to note that the solutions assume an infinite caprock thickness. However, if the thermal front reaches the surface, greater heat exchange between the aquifer and Appendix C, and flowthe caprock is expected, which would reduce the thermal front's advancement rate and velocity values are indicated in the figure-extent.

For demonstration, panels a b of Fig. 4 show  $x_{\rm F}$  and  $r_{\rm F}$  plotted for three different velocities, u, and flow rates, Q. This illustrates the advancement rate of the front decays substantially faster for the radial case (the decay and the derivative of  $r_{\rm F}$  is proportional to  $t^{3/4}$ , compared to the planar case, where it follows  $t^{1/2}$ ). Additionally, in Fig. 4c is shown  $r_{\rm F}$  for conduction only from a point source in an infinite space, demonstrating the low flow rate limit. The inset presents a quasi-steady-state solution of the temperature profile (Stauffer et al., 2014). This scenario is particularly relevant to natural conditions which are often associated with low flow rates (Garven, 1995; Klimchouk et al., 2017).

In this case, the front can becomes quasi-stationary on a timescale of tens of years (Roded et al., 2023) and the reactive front can become nearly stationary, as will be further discussed in the Discussion section below. Lastly, it is recalled that while the solutions assume an infinite caprock thickness, if the thermal front reaches the surface, a greater heat exchange between the aquifer and the caprock is expected, which would reduce the thermal front advancement rate and extension.

#### 785 4. Discussion

765

770

775

780

**Case Studies and Applicability of the** 

#### 4. Discussion and Outlook

#### 4.1. Equilibrium Model Applicability to Hydrothermal Systems

Figure 5 Figure 6 presents an illustrative phase diagram distinguishing between conditions where the THC equilibrium model (Eq. 5) is applicable and those far from equilibrium. The diagram is based on the Damköhler number (Da, which represents the ratio between the characteristic timescales of transport and reaction,  $Da = t_A/t_R = bA/u$ ) and Eq. 1, with the The diagonal line marking the transition at Da > 1 ( $Da_{cr}$ ). Hotter) and hotter colors denote higher Da values and conditions closer to equilibrium. As reactivity ( $1/t_R$ ) increases, the equilibrium model becomes applicable over a wider range of flow velocities, u, or smaller characteristic length scales, l, represented as  $1/t_A = u/l$ . -Here, l represents the local characteristic length scale of thermal and solubility variations (see Appendix A) and accounts for the thermal field effect on reactive transport. Equation 1 assumes first-order kinetics and presents  $Da = l\lambda A/u$ , which is useful for quantifying different fluid-rock interactions that can be approximated as following first-order kinetics.

790

795

800

805

810

The diagram also positions key fluid rock interaction processes according to their characteristic

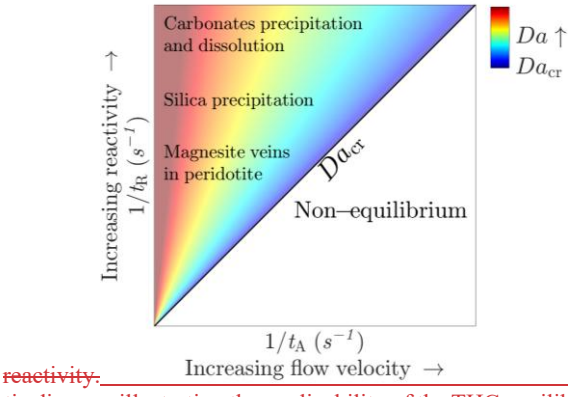


**Figure 6.** A schematic diagram illustrating the applicability of the THC equilibrium model and the positioning of several notable fluid–rock interaction processes according to their typical reactivity. The diagram is plotted based on the characteristic timescales of reaction and transport that define Da, and shows  $1/t_R$  versus  $1/t_A$  ( $Da = t_A/t_R$ ). The equilibrium model can be assumed when  $Da > Da_{cr}$ , with  $Da_{cr}$  defined as a threshold where  $Da_{cr} > 1$ .  $Da_{cr}$  is represented by the diagonal black line on the diagram, with hot colors indicating high Da values and proximity to equilibrium.

Several notable fluid–rock interaction processes are shown on the diagram, positioned according to their characteristic reactivity. At the top are common carbonates, i.e., limestone and dolomite, which typically exhibit high reaction rates and are highly prone to alteration (with values of  $\lambda$ 

typically ranging from 10<sup>-8</sup> to 10<sup>-4</sup> m/s under engineering applications; Dreybrodt et al., 2005; Peng et al., 2015; Plummer et al., 1978).

Silica precipitation is also prevalent in hydrothermal settings (e.g., quartz vein formation and mineral scaling; Glassley, 2014; Huenges and Ledru, 2011; Oliver and Bons, 2001)—At the top are common carbonates, i.e., limestone and dolomite, which typically exhibit high reaction rates and are highly prone to alteration (with  $\lambda$  typically ranging from  $10^{-8}$  to  $10^{-4}$  m/s; Dreybrodt et al., 2005; Peng et al., 2015; Plummer et al., 1978). Silica precipitation is also prevalent in hydrothermal settings (Glassley, 2014; Huenges and Ledru, 2011; Sibson et al., 1975) and is characterized by relatively high reactivity, with a typical rate constant of  $\lambda = 5 \cdot 10^{-10}$  m/s (Rimstidt and Barnes, 1980). In contrast, while non-crystalline silica (amorphous) precipitates relatively quickly, quartz dissolution is typically slower by several orders of magnitude (Rimstidt and Barnes, 1980). An additional interesting behavior associated with quartz occurs at much higher temperatures (e.g.,  $T \geq 300 \,^{\circ}$ C), which can prevail near magmatic intrusions. At these high temperatures, quartz exhibits retrograde solubility, which switches to prograde solubility upon cooling (Glassley, 2014; Scott and Driesner, 2018).

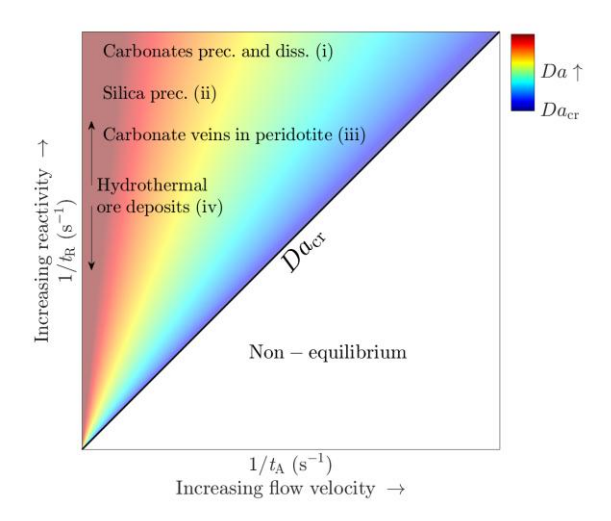


Figure 5. A diagram illustrating the applicability of the equilibrium model and highlighting important fluid rock interaction processes. The Damköhler number is used to differentiate between far from equilibrium conditions and quasi equilibrium, where the equilibrium model can be assumed when  $Da > Da_{cr}$ , with  $Da_{cr}$  defined as a threshold where  $Da_{cr} > 1$ .  $Da_{cr}$  is represented by the diagonal black line on the diagram, with hot colors indicating high Da values and proximity to equilibrium. The diagram is based on Eq. 1 and plots  $1/t_R$  versus  $1/t_A$  (where  $1/t_R = \lambda A_r$  and  $1/t_A = u/l$ ). Main fluid rock interaction processes are indicated on the diagram according to their typical reactivity: (i) carbonate dissolution or precipitation, (ii) silica precipitation, (iii) carbonate vein formation in peridotites, and (iv) hydrothermal ore deposits. In higher reactivity systems, the equilibrium model is applicable under higher flow velocities, and/or small l and relatively large thermal variations, i.e., shorter  $t_{Ar}$ .

The position of these processes on the diagram, as also demonstrated in Section 3.2.1, indicates the applicability of the equilibrium model even at relatively high flow rates. This is especially significant, as high flow rates are characteristic of applications such as groundwater storage and recovery, aquifer thermal storage, and geothermal reinjection (Diaz et al., 2016; Fleuchaus et al., 2018; Maliva, 2019). It is noted that the range of reactivity typically spans several orders of magnitude and is associated with kinetics and large variability in reactive surface area, especially between fractured and porous media (Deng and Spycher, 2019; Maher et al., 2006; Pacheco and Alencoão, 2006; Seigneur et al., 2019).

Additional important settings in which Importantly, the specific reactive surface area,  $A_s$ , (L<sup>2</sup> to L<sup>-3</sup> of porous medium) may vary widely across different rock lithologies, and its effect on the applicability of the equilibrium model is comparable to that of kinetics. Specifically,  $A_s$  can vary, e.g., from  $10^{-1}$  m<sup>-1</sup> in fractured rock (Deng and Spycher, 2019; Pacheco and Van der Weijden, 2014) to above  $10^5$  m<sup>-1</sup> for porous medium (Noiriel et al., 2012; Seigneur et al., 2019) and can also evolve during reactive flow (Noiriel, 2015; Seigneur et al., 2019).

The position of these processes on the diagram, supported by calculations in Section 3.2, demonstrates the applicability of the equilibrium model even at relatively high flow rates. This is especially significant, as high flow rates are characteristic of applications such as groundwater storage and recovery, aquifer thermal storage, and geothermal reinjection (Diaz et al., 2016; Fleuchaus et al., 2018; Maliva, 2019).

Additional important settings where thermally driven reactions may play a significant role include involve mineral carbonation. In particular, this includes the formation of carbonate veins in ultramafic rocks, such as peridotites, by ascending CO2-CO2-rich hydrothermal flow (Kelemen et al., 2011; Menzel et al., 2024). The CO2-rich fluids first dissolve the rock minerals, primarily olivine. Then, as the pH rises and cation enrichment occurs, carbonate precipitation, primarily magnesite, takes place further along the upward flow path. Commonly, the The rate-limiting step in the mineral carbonation process is the commonly suggested to be the relatively slower kinetics of dissolution (Kelemen et al., 2019; Kelemen et al., 2011). compared to precipitation (Hänchen et al., 2006; Kaszuba et al., 2013; Kelemen et al., 2019).

The solubility of olivine is retrograde, as evidenced by the exothermic nature of the reaction (Kaszuba et al., 2013; Prigiobbe et al., 2009). Under these such conditions, the ascending flow along a decreasing geothermal gradient is expected to promote undersaturation, enhance the dissolution reaction (Kelemen et al., 2013), and facilitate. This continued renewal of undersaturation facilitates the development of an extended reactive, thermally driven dissolution front. Considering the typically low rates of ascending hydrothermal flow (e.g.,  $u < 10^{-7}$  m/s; Garven, 1995), along with the relatively rapid characteristic high reaction rates of olivine dissolution kinetics and at high rate constant (Rimstidt, 2015; Rimstidt et al., 2012) temperatures (T > 150 °C; Rimstidt, 2015; Rimstidt et al., 2012), it suggests that Da is can be large. Consequently, mineral carbonation and vein formation occur under quasi equilibrium conditions, making can be controlled by thermally driven solubility changes and described by the THC equilibrium model applicable.

Lastly, a prominent application in which thermally driven reactions play a major role is the hydrothermal formation of ore deposits. These processes involve a wide range of reactions and genetic origins of hydrothermal fluids. Such fluids include metamorphic and meteoric origin waters, which evolve through different fluid fluid or fluid rock interactions, as well as fluids originating directly from magmatic intrusions (so called magmatic hydrothermal fluids; Ingebritsen and Appold, 2012; Robb, 2005). A particularly intriguing phenomenon, often primarily controlled by the dependence of solubility on temperature, is the zoning of metals and minerals, which is commonly observed at various field scales. In these cases, regular belts of different precipitants form progressively as the distance from the hydrothermal fluid source increases. This

pattern is often largely influenced by the solubility of the minerals and their precipitation as a result of cooling along the flow path (Kouzmanov and Pokrovski, 2012; Robb, 2005).

890

895

900

905

910

915

# 4.2. Evolution of Field-seale Development of Thermally Driven Reactive Fronts in Earth Systems

The dominance of the thermal front over the reactive front and their coalescence under quasi-equilibrium conditions allowed for the exploration of the reactive front evolution under different settings, as discussed in Section 3.4. Specifically, the analysis demonstrates that in radial or spherical settings (i.e., flows spreading from a point source) at relatively low flow rates (e.g., several cubic meters per day), a quasi-steady state is achieved over timescales on the order of tens to hundreds of years. Such a cooling process can also induce very steep geothermal gradients. These gradients may be two orders of magnitude larger than the typical basal geothermal gradient formed by Earth heat flow (e.g., 0.025 °C/m; Davies, 2013), as shown in the temperature profile in the inset of Fig. 4c (see also Roded et al. (2023).

A prominent example of such conditions is porphyry type deposits. In these systems, magmatic-hydrothermal fluids are expelled from a crystallizing magmatic intrusion. These fluids then spread away (typically upward and laterally) from the source while cooling and precipitating various metals and minerals (Ingebritsen & Appold, 2012; Robb, 2005). The results here suggest that reactive mineral deposition fronts associated with porphyry ore deposits are essentially stationary for a large part of their lifetime, typically ranging from tens of thousands to millions of years (Cooke et al., 2014; Robb, 2005). The results presented here also contrast with the view that thermal gradients are too weak to promote precipitation (Cooke et al., 2014). Another example involves hypogenic karst and cave formation driven by upwelling hydrothermal flow, which discharges through a permeable fault pathway, spreads radially in a confined aquifer, and cools (Roded et al., 2023, 2024a). In this case, the results suggest that the alteration front or the cave system may exhibit quasi-constant and final dimensions.

However, in the planar case of uniformly ascending hydrothermal flow and mineral carbonation in veins, steady state thermal conditions are presumably reached quickly. This occurs compared to the timescale of vein evolution, which spans tens of thousands of years or longer (Früh Green et al., 2003). Similarly, in any case of hydrothermal ore deposit formation by ascending flow (i.e.,

hypogene), steady state thermal conditions may be reached quickly. In both scenarios, the hot ascending flow alters the background geothermal gradient and may achieve steady state over relatively short timescales (Ingebritsen et al., 2010; Roded et al., 2013).

920

925

930

935

940

945

In these cases, the timescale for the thermal front to reach a steady-state suggests that if reactive processes span periods comparable to the geological timescale of tectonic processes The quasi-equilibrium conditions, characterized by the thermal front's control over the reactive front and their coalescence, allowed examination of their evolution in different settings in Section 3.4. A particularly interesting finding is that in radial (or similar) settings, and at relatively low flow rates, a quasi-steady state develops over brief timescales of tens to hundreds of years. Such a cooling process can also produce very steep thermal gradients, as shown in the temperature profile in Fig. 5d, and can cause localized, thermally driven reactive effects. These thermal gradients may be up to two orders of magnitude greater than the typical geothermal gradient resulting from Earth's heat flow (e.g., ~0.025 °C/m; Turcotte and Schubert, 2014).

A relevant example includes hypogenic karst cave formation driven by upwelling hydrothermal flow through a conduit pathway within a fault. This flow discharges and spreads radially in a confined aquifer while cooling rapidly, promoting localized carbonate dissolution around the water inlet (Roded et al., 2023, 2024a). In this case, the results in Fig. 5d suggest that the cave system or alteration front may reach approximately constant final dimensions. These settings may also apply to additional alterations by hypogenic flows and thermal seepages.

Additional relevant settings that can involve coalesced fronts are ascending hydrothermal flow along a decreasing geothermal gradient, leading to cooling and thermally driven reactions. Particularly, as mentioned above (Section 4.1), this may induce olivine dissolution followed by mineral carbonation in veins in ultramafic rocks. Alternatively, quartz vein formation dominantly occurs due to cooling along the flow path (Bons, 2000; Sibson et al., 1975). In these settings, coalesced fronts may become stationary as the hot ascending flow alters the background geothermal gradient, producing a modified steady vertical thermal profile (Person et al., 1996; Roded et al., 2013).

<u>In these cases, where the coalesced, thermally driven reactive front remains stationary over geological timescales, spatial alterations will depend on these alteration of the front depends on the second of the s</u>

slower tectonic <u>processes</u>. These tectonic timescales. These tectonic timescales are associated with processes such <u>isostasy due toas</u> erosion, subduction, <u>orand</u> orogenic activity. A well-known example is the alteration of the geothermal gradient caused by surface erosion or sediment deposition (Haenel et al., 2012; Turcotte and Schubert, 2002):(Haenel et al., 2012; Turcotte and Schubert, 2014). In response to tectonic changes, the slowly varying subsurface thermal distribution field drives the gradual migration of the reactive front.

# 4.3. 4-Theoretical Modeling Outlook

950

955

960

965

Finally, this study and Roded et al. (2024b) demonstrate the extension of established heat transport solutions to THC-coupled solutions. For future work, the possibility of extending these solutions and approaches in several directions should be investigated. Specifically, it should be examined how the solutions developed can be further extended to address more realistic and complex scenarios. In particular, this includes consideration of more complex kinetic systems involving multiple species and additional or more intricate couplings between variables and parameters.

In such cases, semi-analytical approaches could be especially useful. Due to the quasi-static assumption of reactive flow, the set of equations for reaction rate (Eqs. 10 and 15) or solute disequilibrium (Eqs. B3 and B6) could potentially be implemented in a semi-analytical, coupled, and iterative manner.

Furthermore, the approach taken here and in Roded et al. (2024b) can be adapted to extend additional thermal solutions to significant thermally driven reactive transport scenarios. Notably, this may be especially practical and feasible under the equilibrium assumption, where thermally driven reactions depend solely on the thermal gradients.

# 5. Summary and Conclusions

#### 1. Summary and Conclusions

In this work, the equilibrium assumption iswas used to derive thermally driven reactive transport solutions for the RLP (reactive Reactive Lauwerier problem problem) in both Cartesian and radial coordinates. The solution for porosity evolution is The solutions were then validated and analyzed against a reference solutions and a case study of CO<sub>2</sub> rich hot water injection from a single

well into a carbonate aquifer, leading to cooling and calcite dissolution. The limitations of the solution are analyzed as a function of time and the progression of the thermal front. Under these radial settings, as the studies involving thermally driven reactions of carbonates. In particular, the shortcoming of the equilibrium-approximated solutions associated with the advective boundary condition is analyzed. It was found that as the thermal front advances downstream into regions with lower flow velocity and higher Da, and the error associated with the equilibrium assumption diminishes., inlet temperature gradients become milder and the advective discrepancy less pronounced. This finding motivates also motivated the derivation of a specific eriterion and functional relationship criterion to guidedescribe quasi-equilibrium conditions in the RLP, incorporating which incorporates time and thermal parameters. Specifically, this criterion is expressed through two functions: a dynamic Da number and a thermal parameter function that accounts for front elongation and confirms the interpretation.

Next, the Following this, a unique feature of the thermal front controlling the reactive front and their quasi-equilibrium conditions—the coalescence under quasi-equilibrium conditions—of the thermal and reactive fronts—is used to explore their evolution over time. This is examined in both planar and radial settings, as well as a function of flow rate. The growth rate in the radial case decreases much more rapidly, and it is shown that, in and under the low-flow-rate limit where conduction effectively distributes heat. The advancement rate in the radial case decays much more rapidly, and, notably, in the low-flow-rate limit, the front can become essentially stationary inwithin a relatively very short period. Additionally, under these conditions, very sharp temperature gradients are created near the inlet, which can induce localized fluid-rock interactions.

The applicability of the THC equilibrium model for important notable fluid—rock interaction processes is then discussed and positioned on a diagram based on the Damköhler number, demonstrating the applicability of the equilibrium assumption under different conditions. The processes examined. These include sedimentary reservoir evolution, through reactions involving silica and calcite, as well as natural mineral carbonation in peridotite, and ore deposit formation by hydrothermal flows.ultramafic rocks. These processes are positioned on a phase diagram based on the Damköhler number, illustrating the applicability of the equilibrium model.

Notably, it is suggested that the theoretical approach used here to extend established heat transport solutions to thermally driven reactive transport may be applicable to other important scenarios in <a href="Earth systems"><u>Earth systems.</u></a>. Finally, it is emphasized that <a href="since">since</a> thermally driven reactive fronts <a href="near equilibrium">near equilibrium</a> often <a href="mainbecome">eease to expand after the early stages. Instead, they remainbecome</a> stationary, <a href="with within a short period">with within a</a> short period, their evolution <a href="mainbecome">is</a> governed by geological processes. These processes, such as tectonics or surface erosion and deposition, <a href="mainbecome">oecuroperate</a> on much longer timescales.

# Appendix A: Da Condition for Applicability Underlying Assumptions and Equations of the Equilibrium ModelRLP

This appendix describes the main assumptions of the RLP under the equilibrium assumption. It follows the main presentation from Roded et al. (2024b) and extends it to account for the quasi-equilibrium conditions considered in this study. First, the main assumptions are detailed, followed by a comprehensive overview of the basic conservation equations.

## A.1. Main Model Assumptions

005

010

015

020

025

The thermal Lauwerier (Lauwerier, 1955) solution involves several simplifying assumptions. These include neglecting the initial geothermal gradient and assuming that the basal geothermal heat flux is negligible compared to the heat supplied by the injected fluid. The aquifer is also assumed to be situated at depth, preventing heat from being transferred to the surface; otherwise, there would be greater heat exchange between the aquifer and the caprock. This assumption also depends on the timescale of interest: the thermal front, which rises over time, may not extend to the surface on a short timescale. However, over a longer period, it may transfer heat to the surface, which can be calculated using the characteristic timescale of conduction  $t_C$  ( $t_C = l_C^2/\alpha_b$ , where l accounts for the characteristic length scales of conduction and  $\alpha_b$  is the thermal diffusivity).

In the confining layers, heat is transferred solely through conduction in the vertical direction (z), while neglecting lateral ( $\xi$ ) heat conduction. This assumption restricts the model's applicability to cases with high injected fluid fluxes, where mild lateral temperature gradients evolve. To evaluate the validity of this assumption, a thermal Péclet number is employed, which compares heat advection in the aquifer to lateral heat conduction in the confining layers:  $Pe_T = u_A l/\alpha_b$ , where l is a length scale at which substantial temperature variation occurs (e.g., larger than 2% from the total

temperature change,  $\Delta T$ ). A posteriori inspection confirms that  $Pe_T \gg 1$  beyond the initial moments under all conditions considered here. Moreover, after a very short initial phase, the length scale l should exceed the vertical dimension of the aquifer, H, where complete thermal mixing is assumed  $(l \gg H)$ . This assumption may not hold if a thick aquifer (i.e., large H) is considered, and significant vertical temperature gradients are expected to develop.

Additionally, thermal and solute dispersions within the aquifer are neglected, as both thermal (PeT) and solute (Pes) Péclet numbers are assumed to be large. Properties of the fluid and solid phases, such as density and thermal conductivity, are assumed to be constant and temperature-independent. Finally, it is assumed that Da > 1, making the equilibrium assumption applicable. As a result, reaction rates are essentially independent of kinetics and reactive surface area, as demonstrated in Section 2.2 of the main text.

# A.2. The Basic Conservation Equations

#### **Heat Transport:**

1030

035

040

045

050

Here, the basic conservation equations that underlie the Lauwerier solutions (Eqs. 6 and 13) and the THC equilibrium model (Eq. 5) are presented. More general versions of the conservation equations are provided in Roded et al. (2024b). In what follows, the radial case ( $\xi = r$ ) is considered first, followed by the planar flow case and Cartesian coordinates ( $\xi = x$ ).

Assuming that heat transfer in the radial direction, r, is negligible, the heat equation in the bedrock and caprock confining the aquifer is,

$$\frac{\partial T}{\partial t} = \alpha_{\rm b} \frac{\partial^2 T}{\partial z^2}, \quad \text{for} \quad \begin{cases} z \le -\frac{H}{2} \\ z \ge \frac{H}{2} \end{cases}$$
 (A1)

where *T* denotes temperature, *t* is time, *z* is the vertical coordinate originating at the center of the injection well and *H* denotes the aquifer thickness (see Fig. 1). The thermal diffusivity is given by  $\alpha_b = K_b/Cp_b$ , where the subscript b denotes bulk rock, *K* is the thermal conductivity, and *Cp* is the volumetric heat capacity (Chen and Reddell, 1983; Stauffer et al., 2014).

Assuming that heat transport in the aquifer is dominated by advection and that perfect mixing prevails in the transverse direction (z), a 'depth-averaged' heat transport equation can be derived for the aquifer domain:

$$C_{\mathrm{p_b}}H\frac{\partial T}{\partial t} = -C_{\mathrm{p_f}}H\frac{1}{r}\frac{\partial (ruT)}{\partial r} - \boldsymbol{n} \cdot \boldsymbol{\Theta}(r,t), \quad \text{for} \quad -\frac{H}{2} \le z \le \frac{H}{2}, \tag{A2}$$

where subscript f denotes fluid and u is the Darcy flux, assumed to be uniform along the z direction, and calculated from the total volumetric flow rate, Q, using  $u(r) = Q/(H2\pi r)$  (Andre and Rajaram, 2005; Lauwerier, 1955). The  $\Theta$  function accounts for the heat exchange between the aquifer and the confining bedrock and caprock, calculated using Fourier's law, assuming continuous temperature at the interfaces:

$$\mathbf{\Theta} = -2K_{\rm b} \frac{\partial T}{\partial z} \Big|_{z=\frac{H}{2}, -\frac{H}{2}}.$$
(A3)

The factor of two accounts for both the bedrock and caprock (Stauffer et al., 2014). In Eq. A2\_n represents a unit vector directed outward from the aquifer and perpendicular to the interface between the aquifer and the bedrock or caprock. This orientation ensures that, e.g., in the case of a warmer aquifer, the upward and downward heat fluxes constitute a heat sink.

## **Reactive Transport:**

055

060

065

075

The solute advection-reaction equation in the aquifer is:

070 
$$0 = -u\frac{\partial c}{\partial r} - \Omega(r, t), \text{ for } -\frac{H}{2} \le z \le \frac{H}{2},$$
 (A4)

where c is the solute concentration and  $\Omega$  is the reaction rate (Chaudhuri et al., 2013; Szymczak and Ladd, 2012). Note that the transient and dispersivity terms in Eq. A4 are neglected, with the latter being omitted due to the assumption of  $Pe_s \gg 1$ . The justification for neglecting the transient term and invoking the quasi-static approximation in the derivation of Eq. A4, lies in the separation of timescales between the relaxation of solute concentration ( $t_A$ ), heat conduction ( $t_C$ ) in the confining rocks and mineral alteration (for in-depth analysis and discussion see Roded et al. (2024b) and as well, e.g., Bekri et al., 1995; Ladd and Szymczak, 2017; Lichtner, 1991; Roded et al., 2020).

Using the reaction rate, the change in porosity,  $\theta$ , can be calculated as:

$$\frac{\partial \theta}{\partial t} = -\frac{\Omega}{v c_{\text{sol}}}, \quad \text{for} \quad -\frac{H}{2} \le z \le \frac{H}{2}.$$
(A5)

Here,  $c_{sol}$  represents the concentration of soluble solid mineral and v accounts for the stoichiometry of the reaction. For planar flow and Cartesian coordinates, r can be substituted with x in the equations above, and Eq. A2 then takes the following form:

$$C_{\mathrm{p_b}}H\frac{\partial T}{\partial t} = -uC_{\mathrm{p_f}}H\frac{\partial T}{\partial x} - \boldsymbol{n}\cdot\boldsymbol{\Theta}(x,t), \quad \text{for} \quad -\frac{H}{2} \leq z \leq$$

H/2. Assuming quasi-equilibrium conditions and equating the

reaction rates given in Eqs. 6 and 14 yields,

$$u \frac{\partial c_s(T)}{\partial r} \approx A_s \lambda (c - c_s(T)).$$
 (A.1)

Assuming on a local scale that

085

100

$$\frac{\partial c_{\varepsilon}}{\partial r} \approx \frac{\Delta c_{\varepsilon\varepsilon}}{l},$$
 (A.2)

where, l represents a characteristic length scale over which temperature and solubility change, with the magnitude of  $\Delta c_{se}$  is  $c\Delta c_s$ , where c << 1 (e.g., c = 0.01) and  $\Delta c_s$  denotes the absolute solubility change in the system ( $\Delta c_s = |c_s(T_{in}) - c_s(T_0)|$ ). Assuming quasi-equilibrium conditions and that  $\Delta c_{se}/(c - c_s(T)) > 1$ , Eq. A.1 can be rearranged to give,

$$Da = \frac{lA_s\lambda}{lL_s} > 1,\tag{A.3}$$

where *Da* is the Damköhler number, and the velocity *u* is replaced by the characteristic fluid velocity *u*<sub>A</sub> in the above equation.

(A6)

The above set of heat transport equations underlies the development of the thermal Lauwerier solutions presented in Section 3.1 (Eqs. 6 and 13). Section 2.2 of the main text provides the derivation of the equilibrium-approximated form of Eq. A4, which is used to obtain the equilibrium-approximated solutions developed in this study.

# Appendix B: RLP Solutions

# **B.1. Radial RLP Solutions**Case

The RLP solution to the RLP for the solute disequilibrium in the radial case is given by,

1105  $\Lambda = \Delta T \beta e^{\left(\frac{\eta^2}{4\zeta^2} - \eta r^2\right)} \left( \text{erf} \left[ \zeta r^2 - \frac{\eta}{2\zeta} \right] + \text{erf} \left[ \frac{\eta}{2\zeta} \right] \right). \tag{B.1,}$ 

where  $\eta = \pi H A_s \lambda / Q$  and the definition of  $\zeta$  is given in Eq. 7.

A closed-form expression for the temporal and spatial evolution of porosity,  $\theta$ , is given by,

(B1)

$$\begin{split} \theta(r,t) &= \theta_0 + 4 \frac{\zeta^2 t}{\eta^2} \frac{\lambda A_{\rm s} \Delta T \beta}{\nu c_{\rm sol}} \bigg( -e^{\eta/4 \left(\frac{\eta}{\zeta^2} - 4r^2\right)} \bigg) \bigg( \text{erf} \left[ \zeta r^2 - \frac{\eta}{2\zeta} \right] + \text{erf} \left[ \frac{\eta}{2\zeta} \right] \bigg) + \frac{\eta}{\zeta \sqrt{\pi}} e^{-\eta r^2} \\ &+ \text{erf} [\zeta r^2] (1 - \eta r^2) - \frac{\eta}{\zeta \sqrt{\pi}} e^{-\zeta^2 r^4} + \eta r^2 \\ &- 1 \bigg). \end{split}$$

For efficient computation and preventing integer overflow (Press et al., 2007), an approximate solution of Eq. B.1For efficient computation and preventing integer overflow, an approximate solution of Eq. B1 is developed using the first-order asymptotic expansion of erfc,

$$\Lambda = \frac{\Delta T \beta}{\sqrt{\pi}} e^{(-\eta r^2)} \left( \frac{e^{(\eta r^2 - \zeta^2 r^4)}}{\frac{\eta}{2\zeta} - \zeta r^2} - \frac{2\zeta}{\eta} \right). \tag{B.3}$$

# **B.2.** Planar Case

115

For the planar case, the corresponding solutions are given by,

120 
$$\Lambda = \Delta T \beta e^{\left(\frac{\sigma^2}{4\omega^2} - \sigma x\right)} \left( \text{erf} \left[ \omega x - \frac{\sigma}{2\omega} \right] + \text{erf} \left[ \frac{\sigma}{2\omega} \right] \right), \tag{B4}$$

and

130

135

140

$$\theta(x,t) = \theta_0 + 4 \frac{\omega^2 t}{\sigma^2} \frac{\lambda A_s \Delta T \beta}{\nu c_{sol}} \left( -e^{\sigma/4 \left( \frac{\sigma}{\omega^2} - 4x \right)} \left( \text{erf} \left[ \omega x - \frac{\sigma}{2\omega} \right] + \text{erf} \left[ \frac{\sigma}{2\omega} \right] \right) + \frac{\sigma}{\omega \sqrt{\pi}} e^{-\sigma x} + \text{erf} \left[ \omega x \right] (1 - \sigma x) - \frac{\sigma}{\omega \sqrt{\pi}} e^{-\omega^2 x^2} + \sigma x - 1 \right).$$
(B5)

An approximate expression for Eq. B4 is given by

25 
$$\Lambda = \frac{\Delta T \beta}{\sqrt{\pi}} e^{(-\sigma x)} \left( \frac{e^{(\sigma x - \omega^2 x^2)}}{\frac{\sigma}{2\omega} - \omega x} - \frac{2\omega}{\sigma} \right). \tag{B6}$$

Here,  $\sigma = A_s \lambda / u$  and the definition of  $\omega$  is given in Eq. 14.

To prevent integer overflow errors, Eq. B.3 is Eqs. B3 and B6 are used to calculate the undersaturation and profiles shown in Figs. 2b and 3b, and the reaction rate profiles in Fig. 4a. These expressions are Figs. 2b and 3a, respectively. It is also used to iteratively solve numerically in the iterative numerical solution to obtain the porosity profile at later times, as shown in Fig. Figs. 2c and 3c (t = 100 kyr). The accuracy of the approximation in Eq. B.3 was validated by comparing it with the full solution in Eq. C.1, which is solvable for early times ( $t \approx 1 \text{ yr}$ ). Additionally, Prior validation confirmed the accuracy of Eq. C.3 and the iterative solutions was also validated by solving for the porosity profile and comparing the results to those obtained using the full solution in Eq. B.2 for t = 10 kyrapproximate solutions (Eqs. B3 and B6; (Roded et al., 2024b).

# **Appendix C: Derivation of the Applicability Criterion**

In this appendix, the derivation of the applicability criterion shown in Section 3.3 is presented. This criterion provides a functional relationship between key parameters, variables, and the system equilibrium state in RLP settings. The derivation of the criterion leverages a key feature of the quasi-equilibrium regime: the coalescence of the thermal and reactive fronts in the aquifer, which occurs when *Da* is high (compare the curves in Fig. 2a and b). In this regime, reactions dominate over transport, and thermally induced disequilibrium dissipates rapidly, essentially not extending downstream of the thermal front.

- It is noted that even when the fronts coincide downstream, far-from-equilibrium conditions may still persist upstream. This is observed in the results of Fig. 4, where the equilibrium solution (which aligns with the thermal front) and the reference solution closely match downstream at later times, but diverge upstream. Nonetheless, the derived functional relationships offer useful guidance.
- First, the thermal front's outer-end position,  $\xi_F(t)$ , is defined as the furthest distance of thermal perturbation due to the injection at a given time. The thermal perturbation is quantified by  $\varepsilon = \frac{(T(\xi_F) T_0)/\Delta T}{\epsilon}$ , where  $\varepsilon$  is a prescribed small value ( $\varepsilon \ll 1$ ); here,  $\varepsilon = 0.01$ . Below, we consider the radial case ( $\xi_F = r_F$ ), though applying the same steps to the planar case equations yields the same result.
- Rearranging and substituting the definition of  $\varepsilon$  into the Lauwerier solution (Eq. 6) yields:

$$\varepsilon = \operatorname{erfc}(a)$$
, where  $a = \zeta(t)r_{\rm F}^2$ , (C1)

where a is a constant, and for  $\varepsilon = 0.01$ ,  $a \approx 1.8$ . Then,  $r_F$  can be expressed as,

160

$$r_{\rm F} = \sqrt{\frac{a}{\zeta(t)}}.$$
(C2)

- Next, an approximate form of the reference solution for disequilibrium is used (Eq. B3 in Appendix B; Roded et al., 2024b). The reasoning for using a far-from-equilibrium-based solution, even though the equilibrium model strictly assumes  $\Lambda = 0$  (cf. Eqs. 4 and 5), is that a small  $\Lambda$  confirms the validity of this approximation. Therefore, solute disequilibrium serves as a metric to quantify the spatial and temporal extent over which the equilibrium assumption is valid.
- Assuming quasi-equilibrium at the front's outer-end position,  $r_F$ , and applying the condition  $\varepsilon \ge \Delta/\Delta c_s$ , where  $\Delta c_s$  denotes the solubility change in the system,  $\Delta c_s = c_s(T_{in}) c_s(T_0)$ , which here may be positive or negative, Eq. B3 becomes:

$$\varepsilon \ge \frac{\Delta T}{\Delta c_{\rm s}} \frac{\beta}{\sqrt{\pi}} e^{(-\eta r_{\rm F}^2)} \left( \frac{e^{(\eta r_{\rm F}^2 - \zeta^2 r_{\rm F}^4)}}{\frac{\eta}{2\zeta} - \zeta r_{\rm F}^2} - \frac{2\zeta}{\eta} \right). \tag{C3}$$

Next, applying a few more steps by substituting the definition from Eq. C2, neglecting early times, and assuming high Da and  $\eta \gg \zeta$ , Eq. C3 can be simplified to:

170 
$$\varepsilon \ge \frac{\Delta T}{\Delta c_s} \frac{\beta}{\sqrt{\pi}} \frac{2\zeta}{\eta}$$
. (C4)

Noting that  $\beta = \Delta c_s/\Delta T$  and explicitly substituting the parameters using Eq. 7 and  $\eta = \pi H A_s \lambda/Q$ , Eq. C4 becomes,

$$1 \gg \frac{2}{\sqrt{\pi t}} \left( \frac{1}{A_{\rm s} \lambda} \right) \left( \frac{\sqrt{K_{\rm b} C_{\rm p_b}}}{H C_{\rm p_f}} \right), \tag{C5}$$

where  $A_s$  is the specific reactive area [L<sup>-1</sup>] and  $\lambda$  is the kinetic reaction rate coefficient of the first-order reaction [L T<sup>-1</sup>]. Equation C5 defines the conditions under which the thermal and reactive fronts coincide and provides a functional relationship to the equilibrium state in RLP settings.

#### **Appendix D: Parameter Values**

175

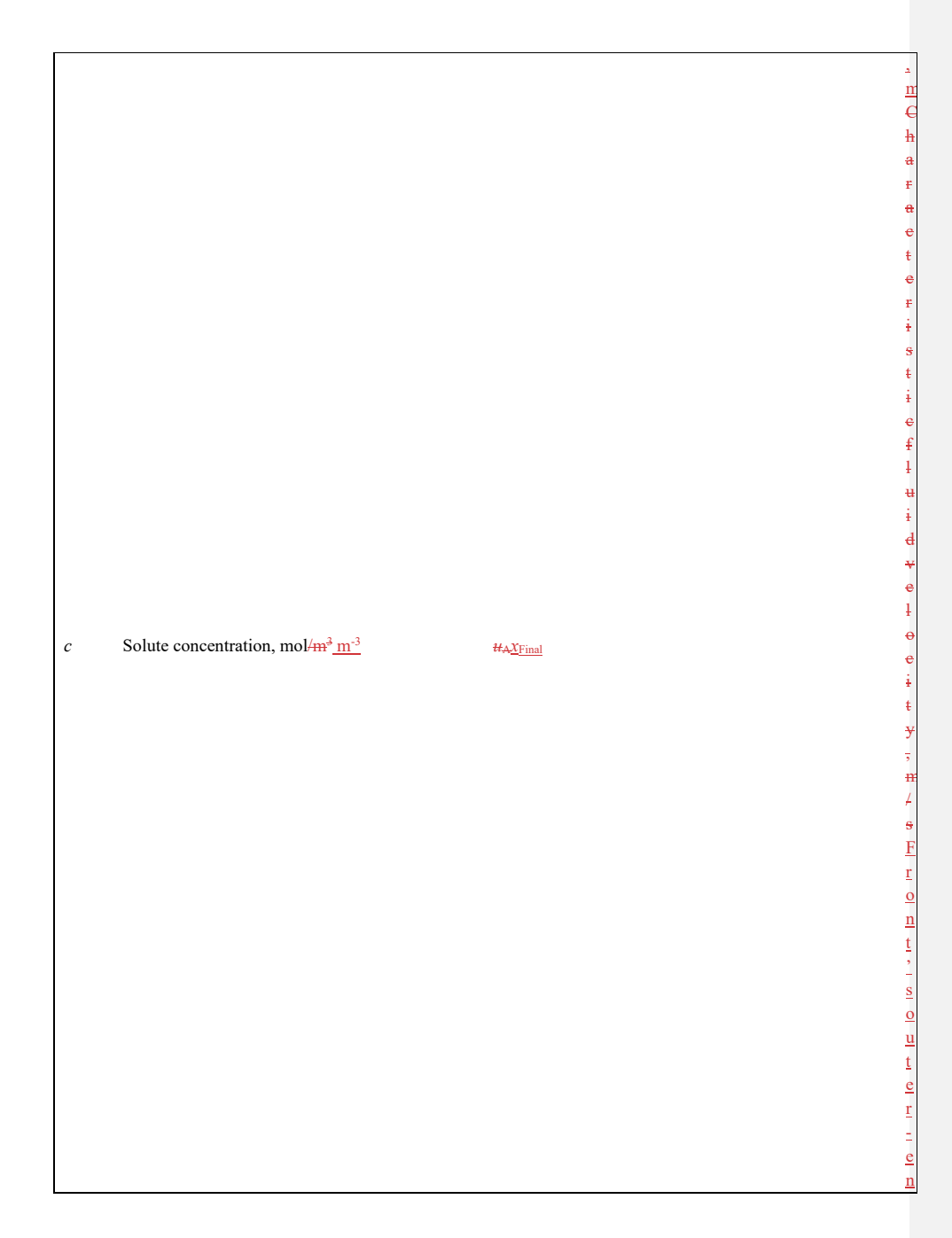
180

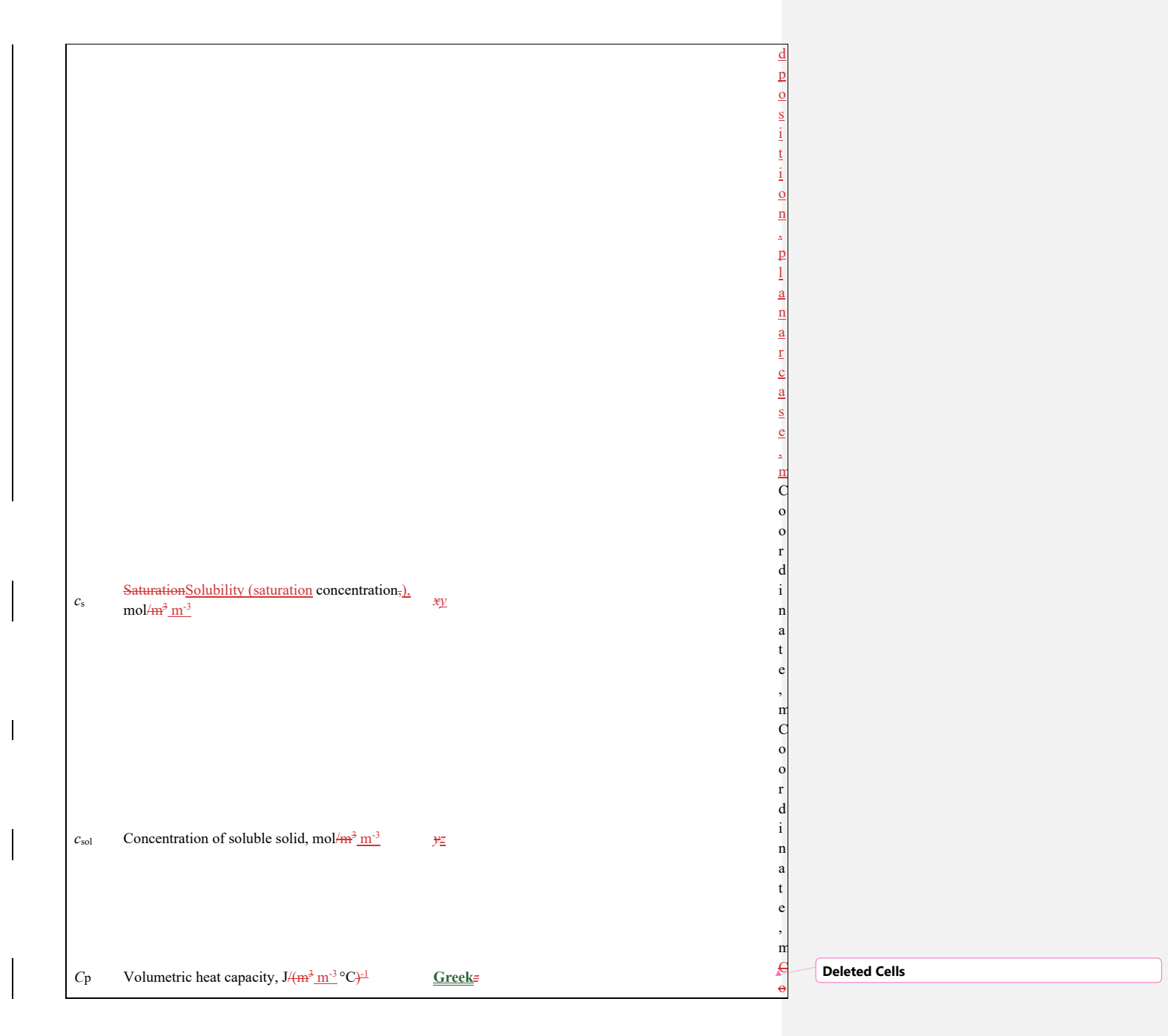
Table 1. Parameter values used in the simulation in Section 3.2.	<del>1.</del>	
Table 1. Parameter values used in the simulation in Section 3.2.		
Aquifer thickness	H=4  m	
Initial porosity	$\theta_0 = 0.05$	
Total volumetric flow rate <sup>1</sup>	$Q = 500 \text{ m}^3 / \text{s} \frac{\text{day}^{-1}}{\text{s}}$	
Fluid velocity	$u = 10^{-6} \text{ m s}^{-1}$	
Initial aquifer temperature <sup>2</sup>	$T_0 = 20  ^{\circ}\mathrm{C}$	
Injection temperature <sup>2</sup>	$T_{\rm in} = 60  ^{\circ}{\rm C}$	
Fluid volumetric heat capacity <sup>2</sup>	$C_{\rm pf} = 4.2 \cdot 10^6 \mathrm{J \ m^{-3} \cdot oC^{-1}}$	
Rock volumetric heat capacity <sup>2</sup>	$C_{\text{pb}} = 3.12 \cdot 10^6 \text{ J/(m}^3 \text{ m}^{-3}  ^{\circ}\text{C})^{-1}$	
Rock thermal conductivity <sup>2</sup>	$K_{\rm b} = 3 \text{ W m}^{-1} - {\rm ^{\circ}C^{-1}}$	
Calcite rate coefficient <sup>3</sup>	$\lambda = 10^{-6} \text{ m/s}$	
Fractured carbonates specific reactive surface area <sup>5</sup>	$A_{\rm s}=10~{\rm m}^{-1}$	
Calcite mineral concentration <sup>3</sup>	$c_{\rm sol} = 2.7 \cdot 10^4  \text{mol/m}^3  \underline{\text{m}}^{-3}$	
Solubility change parameter calcite <sup>7</sup>	$\beta = -0.075 \text{ mol m}^{-3} ^{\circ}\text{C}^{-1}$	
Stoichiometry coefficient <sup>3,4</sup>	v = 1	

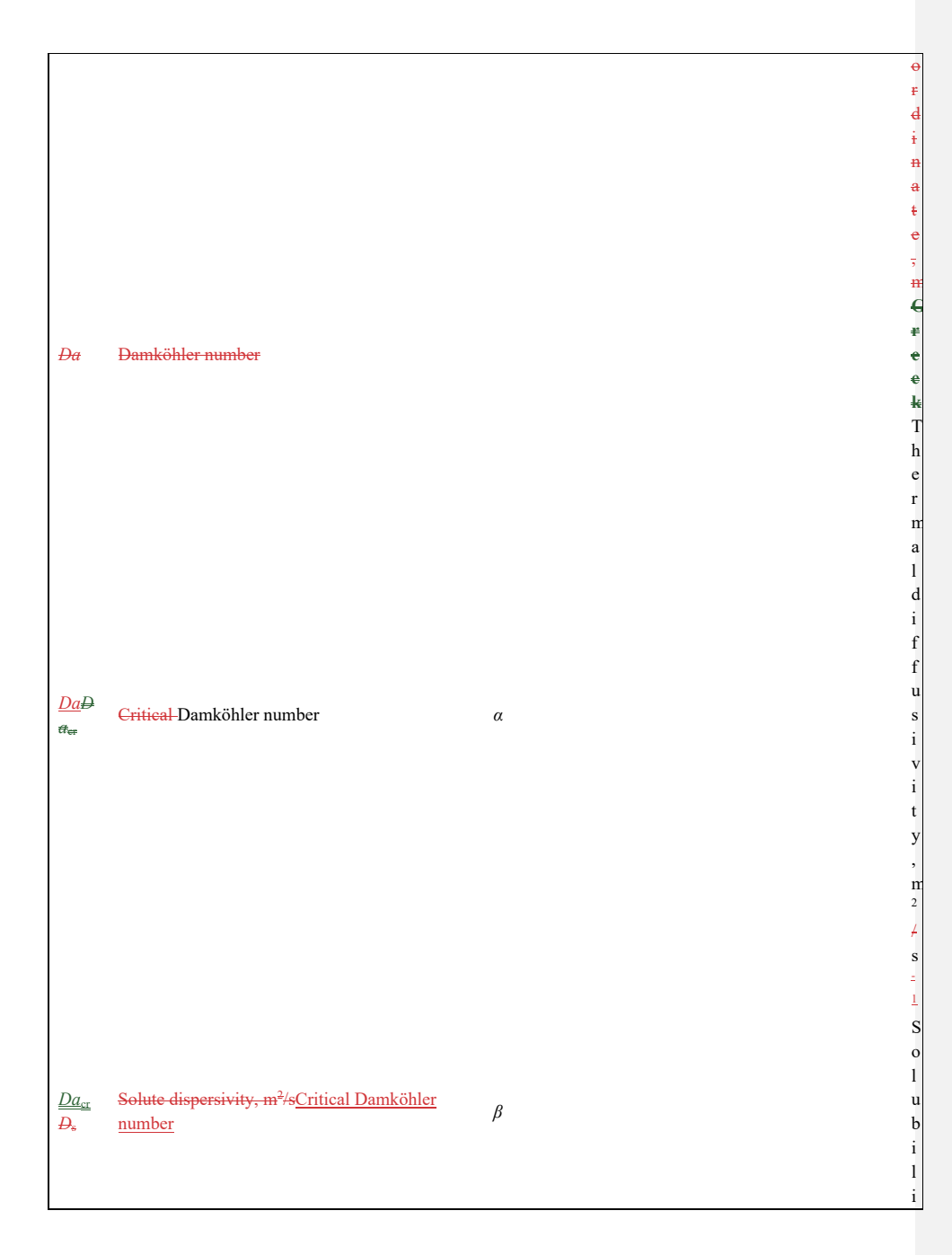
1-Glassley (2014)Glassley (2014); 2-Huenges and Ledru (2011); 3-Palmer (1991); 4-Rimstidt and Barnes (1980); 5-see textSection 4.1; 6-Hussaini and Dvorkin (2021) and Lai et al. (2015); 7-Roded et al. (2023).

a	Error function argument,	$T_{\underline{X}}$
$A_{ m s}$	Specific reactive surface area, m <sup>2</sup> /m <sup>3</sup> m <sup>-3</sup>	# <u>X</u> E

	d
	¥
	e
	ł
	0
	e
	i
	ŧ
	y
	5
	n
	+
	S
	<u>r</u>
	Ī
	n
	± t
	,
	s
	0
	u
	ţ
	<u>e</u>
	r
	Ξ
	<u>e</u>
	<u>n</u>
	<u>d</u>
	p
	0
	<u>2</u>
	± t
	i
	0
	n
	2
	р
	1
	<u>a</u>
	<u>n</u>
	<u>a</u>
	<u>r</u>
	C
	<u>d</u>
	d v e l e e : t t y ; m / s F r o n t ; - s o u t e r - e n d p o s i i t i o n - p l a n a r c a s e
	×

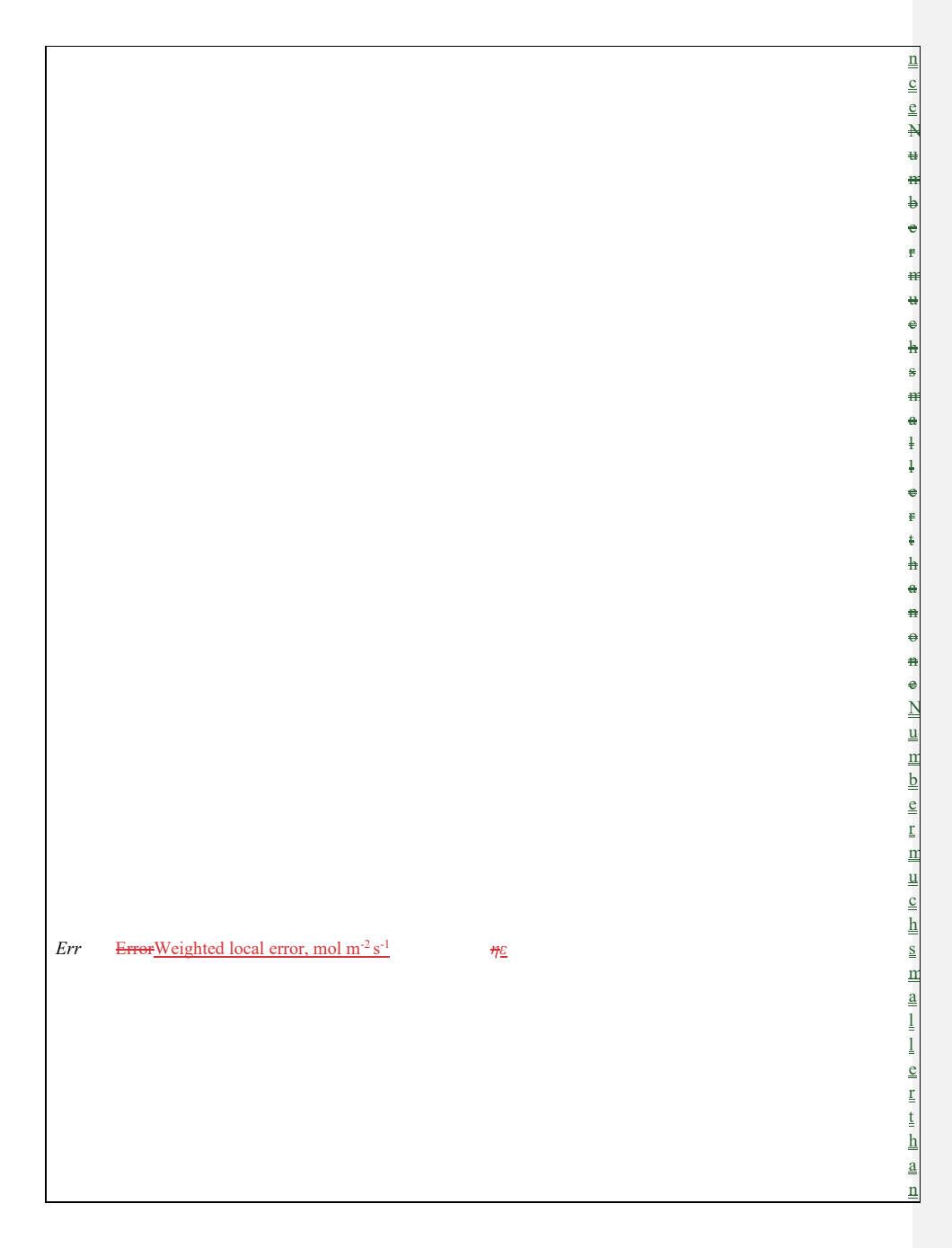


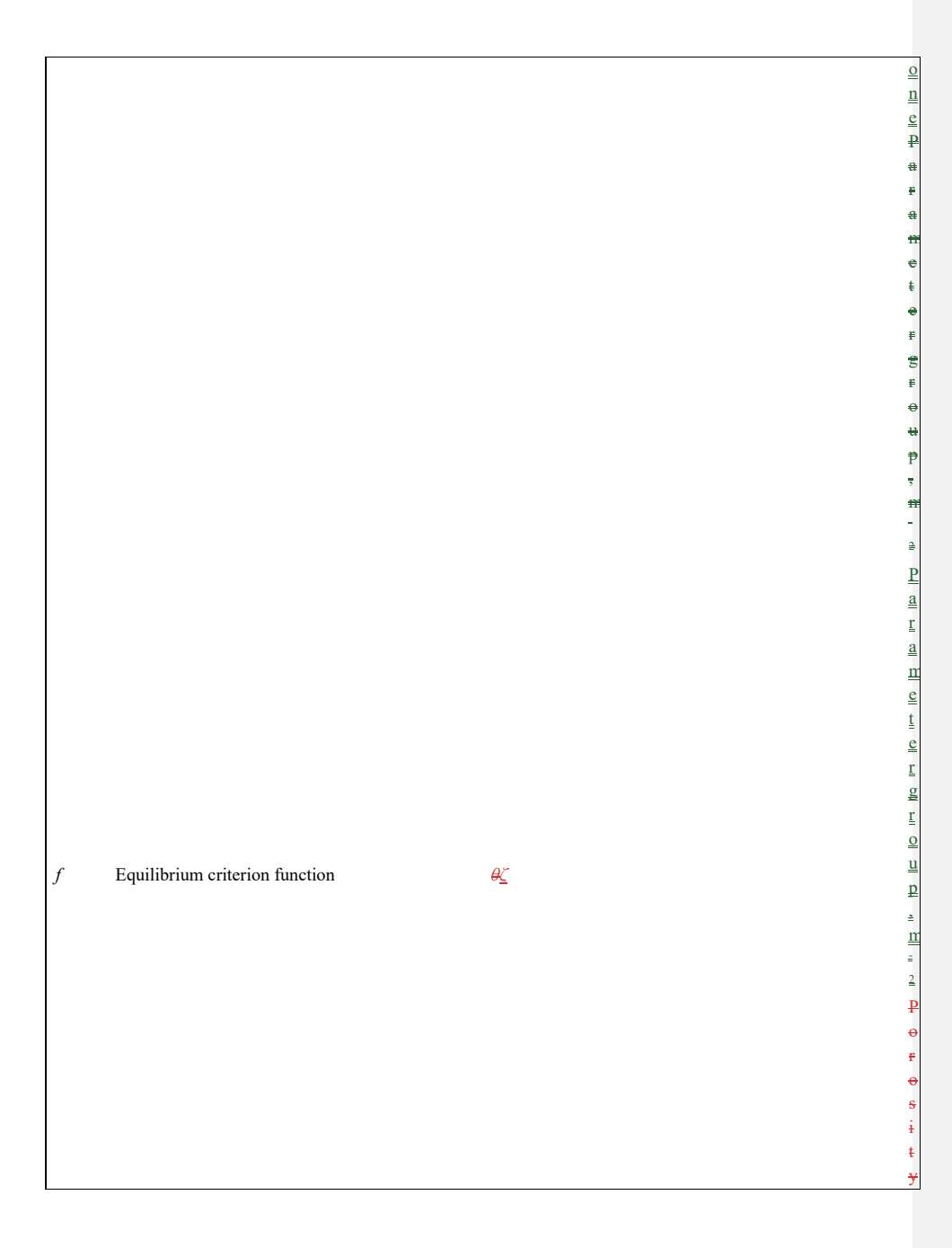




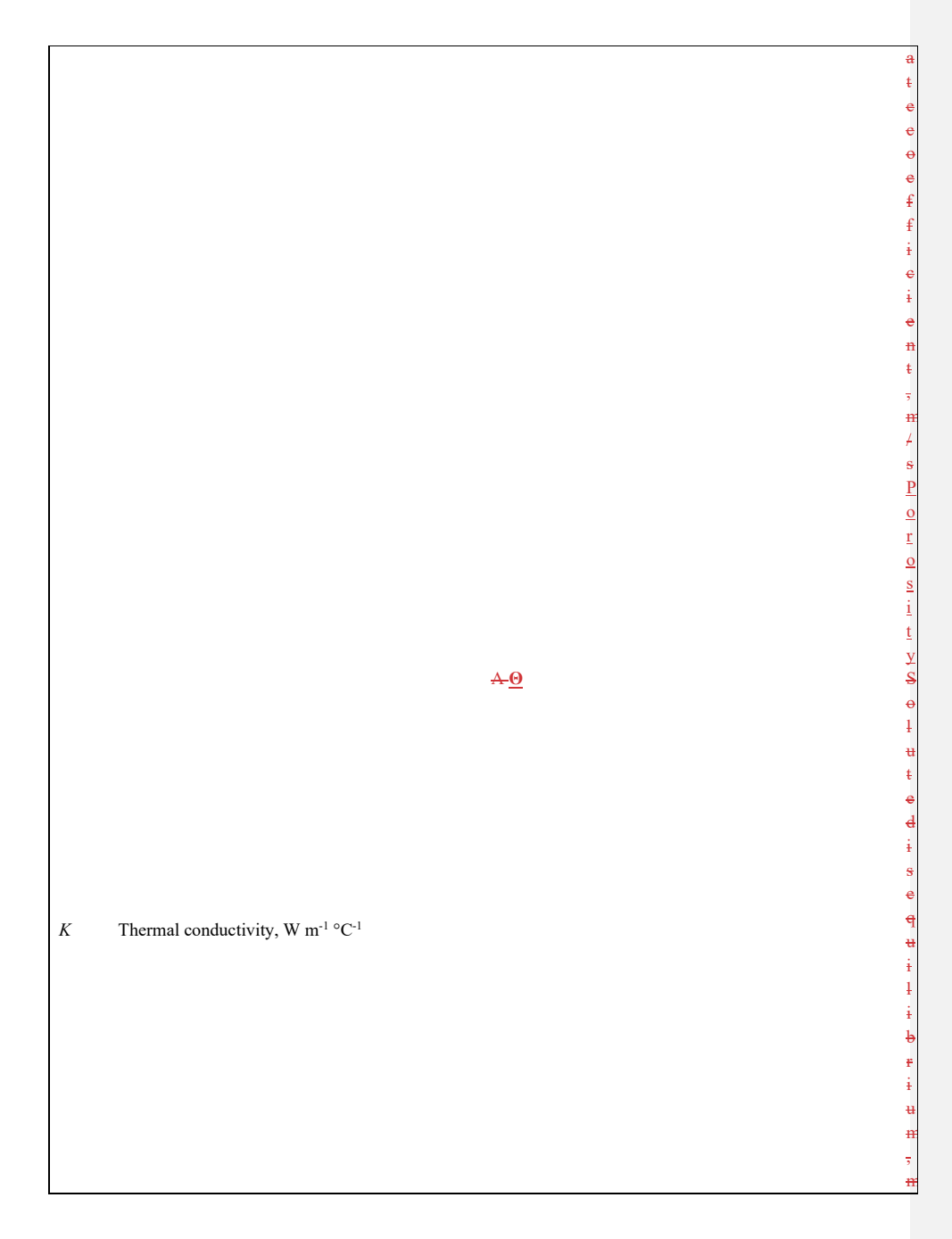
 $D_{\mathbb{T}}$ Thermal dispersivity, m<sup>2</sup>/s

 $\Delta c_{\rm ss} \underline{\Gamma}$ Error function Complementary error function  $\epsilon \Delta$ 

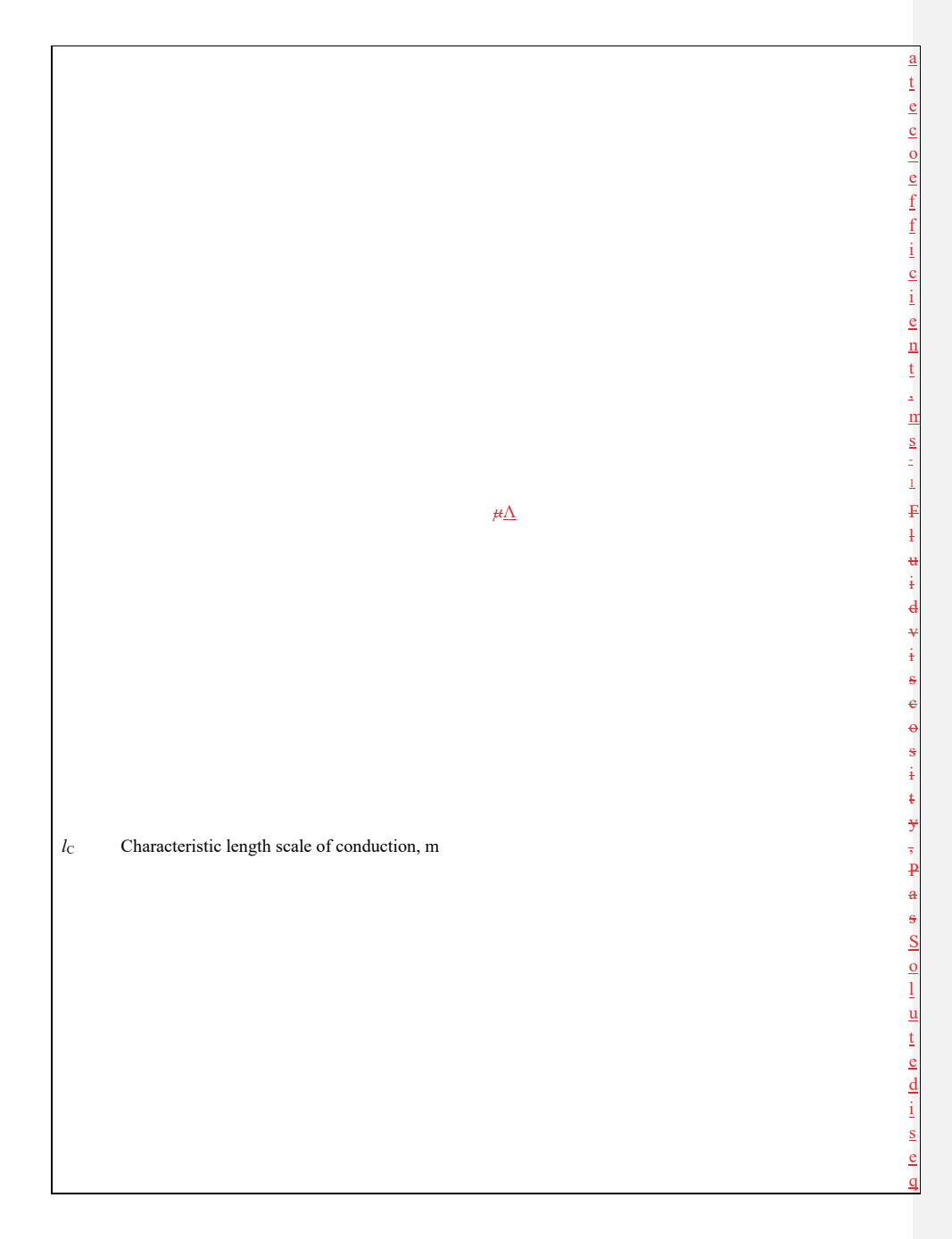




Equilibrium criterion function  $\Theta \underline{\eta}$ HAquifer thickness, m  $\lambda \underline{\theta}$ 







n Unit vector, m

Fluid pressure, Pa

$Pe_{s}$	Solute Péclet number	ξ
$Pe_{ m T}$	Thermal Péclet number	⇔≚̃E

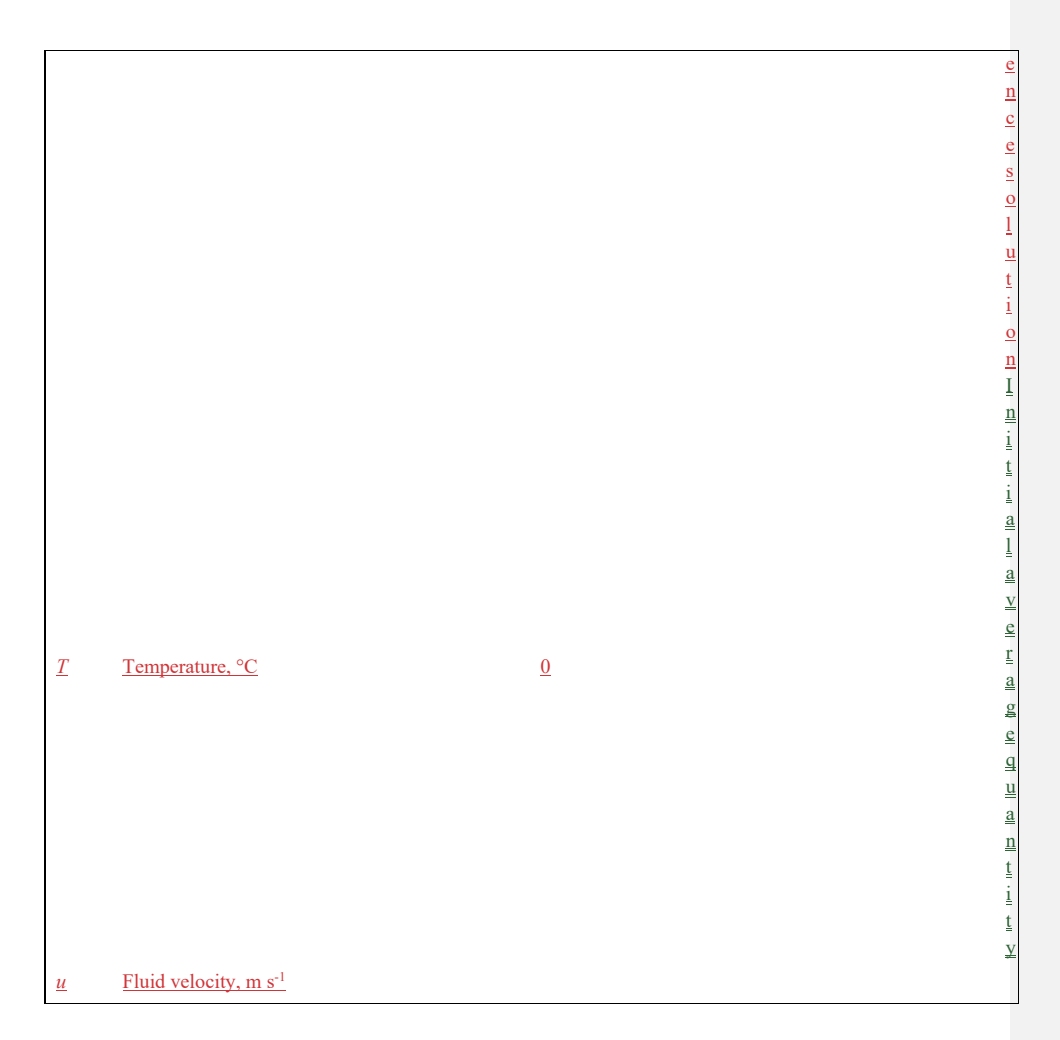
Total volumetric flow rate, m<sup>3</sup>/s day<sup>-1</sup>  $\Omega_{\underline{\sigma}}$ 

r	Coordinate, m	<u>@</u>	



			е
			θ 1
			u
			ŧ
			i
			е
			Đ
	E ( 11 2 1		1
<b>X</b> E	Front end location, planar case, m		u
			i
			d
			Į
			Ħ
$X_{\mathbb{F}}$	Final front end location, planar case, m	in	ļ
			e
			ŧ
			E
			u
			1
			k
١.	T.'	1	ŗ
t	Time, s	max <u>b</u>	<u>o</u>
			C
			k N
			A
			a
			X
			₽
			e
			£
			e
			F
			e
			Ħ
			e
			e
t'	Time parameter, s	<u>RefEqu</u>	Ŀ
			<u>e</u> <u>E</u> <u>g</u> <u>u</u> <u>i</u>
			u
			i
			1
			<u>i</u> <u>b</u> <u>r</u> <u>i</u>
			r
			i
			<u>u</u>
L			<u>n</u>

			s
			o
			1
			u
			ţ
			i
			o
			n
			<u>F</u> <u>I</u>
			1
			<u>u</u>
			<u>u</u> <u>i</u> d
			<u> </u>
			n
			÷
			ŧ
			:
			#
			1
			e
$t_{\rm A}$	Characteristic timescale of advection, s	$\Theta \underline{\mathbf{f}}$	*
			•
			¥
			<del>a</del>
			<del>g</del>
			e
			9
			ŧ
			<del>a</del>
			<del>11</del>
			<b>.</b>
			•
			<b>.</b>
			<del>)</del> 1
			<u>I</u>
$t_{\rm C}$	Characteristic timescale of conduction, s	<u>in</u>	<u>n</u> 1
10	characteristic timescare of conduction, s	<u> </u>	<u> </u>
			1
<u>t</u> Lg	Thermal retardation time, s		<u>e</u> <u>t</u> <u>N</u>
-LEE	<del></del>	max	a
			x
			<u>a</u> x <u>R</u> <u>e</u> <u>f</u>
			<u>e</u>
<u>t</u> <u>R</u>	Characteristic timescale of reaction, s	Ref	$\overline{\mathbf{f}}$
			<u>e</u>
L			<u>r</u>



## Code & Data availability:

The MATLAB codes and data generated in this study are available to reviewers and upon request from the author.

## 1195 Competing interests:

The author declares no competing interests.

#### **Acknowledgments:**

The research was supported as part of the Center on Geo-processes in Mineral Carbon Storage, an Energy Frontier Research Center funded by the U.S. Department of Energy (DOE), Office of Science, Basic Energy Sciences (BES), under Award # DE-SC0023429.

#### References

1200

Anderson, R.: Infectious diseases of humans: dynamics and control, Oxford University Press, 1991.

Andre, B. J. and Rajaram, H.: Dissolution of limestone fractures by cooling waters: Early development of hypogene karst systems, Water Resour. Res., 41, 2005.

1205 Appelo, C. A. J. and Postma, D.: Geochemistry, groundwater and pollution, CRC press, 2004.

Bekri, S., Thovert, J. F., and Adler, P. M.: Dissolution of porous media, Chem Eng Sci, 50, 2765–2791, 1995.

Bons, P. D.: The formation of veins and their microstructures, J. Virtual Explor., 2, 12, 2000.

Chadam, J., Hoff, D., Merino, E., Ortoleva, P., and Sen, A.: Reactive infiltration instabilities, IMA J. Appl. Math., 36, 207–221, 1986.

1210 Chaudhuri, A., Rajaram, H., and Viswanathan, H.: Early-stage hypogene karstification in a mountain hydrologic system: A coupled thermohydrochemical model incorporating buoyant convection, Water Resour. Res., 49, 5880– 5899, 2013.

Chen, C. and Reddell, D. L.: Temperature distribution around a well during thermal injection and a graphical technique for evaluating aquifer thermal properties, Water Resour. Res., 19, 351–363, 1983.

215 Cooke, D., Hollings, P., Wilkinson, J., Tosdal, R., and Turekian, H.: 13.14 Geochemistry of porphyry deposits, Treatise Geochem., 13, 357–381, 2014.

Cornish-Bowden, A.: Fundamentals of enzyme kinetics, John Wiley & Sons, 2013.

Corson, L. T. and Pritchard, D.: Thermosolutal convection in an evolving soluble porous medium, J. Fluid Mech., 832, 666-696, 2017.

1220 Coudrain-Ribstein, A., Gouze, P., and de Marsily, G.: Temperature-carbon dioxide partial pressure trends in confined aquifers, Chem. Geol., 145, 73–89, 1998.

Craw, D.: Fluid flow at fault intersections in an active oblique collision zone, Southern Alps, New Zealand, J. Geochem. Explor., 69, 523–526, 2000.

Davies, J. H.: Global map of solid Earth surface heat flow, Geochem. Geophys. Geosystems, 14, 4608-4622, 2013.

1225 Deng, H. and Spycher, N.: Modeling reactive transport processes in fractures, Rev. Mineral. Geochem., 85, 49–74, 2019.

Deng, H., Molins, S., Steefel, C., DePaolo, D., Voltolini, M., Yang, L., and Ajo-Franklin, J.: A 2.5 D reactive transport model for fracture alteration simulation, Environ. Sci. Technol., 50, 7564–7571, 2016.

Diaz, A. R., Kaya, E., and Zarrouk, S. J.: Reinjection in geothermal fields—A worldwide review update, Renew. Sustain. Energy Rev., 53, 105–162, 2016.

Dreybrodt, W., Gabrovšek, F., and Romanov, D.: Processes of Speleogenesis: A Modeling Approach, Založba ZRC, 2005.

Etiope, G.: Natural gas seepage, Earth's Hydrocarb. Degassing, 199, 2015.

1230

Fleuchaus, P., Godschalk, B., Stober, I., and Blum, P.: Worldwide application of aquifer thermal energy storage–A review, Renew. Sustain. Energy Rev., 94, 861–876, 2018.

Früh-Green, G. L., Kelley, D. S., Bernasconi, S. M., Karson, J. A., Ludwig, K. A., Butterfield, D. A., Boschi, C., and Proskurowski, G.: 30,000 years of hydrothermal activity at the Lost City vent field, Science, 301, 495–498, 2003.

Furui, K., Abe, T., Watanabe, T., and Yoshioka, K.: Phase-field modeling of wormhole formation and growth in carbonate matrix acidizing, J. Pet. Sci. Eng., 209, 109866, 2022.

Garven, G.: Continental-scale groundwater flow and geologic processes, Annu. Rev. Earth Planet. Sci., 23, 89-117, 1995.

Glassley, W. E.: Geothermal energy: renewable energy and the environment, CRC press, 2014.

Haenel, R., Stegena, L., and Rybach, L.: Handbook of terrestrial heat-flow density determination: with guidelines and recommendations of the International Heat Flow Commission, Springer Science & Business Media, 2012.

Hidalgo, J. J., Fe, J., Cueto-Felgueroso, L., and Juanes, R.: Scaling of convective mixing in porous media, Phys. Rev. Lett., 109, 264503, 2012.

Hänchen, M., Prigiobbe, V., Storti, G., Seward, T. M., and Mazzotti, M.: Dissolution kinetics of fosteritic olivine at 90–150 C including effects of the presence of CO2, Geochim. Cosmochim. Acta, 70, 4403–4416, 2006.

Huenges, E. and Ledru, P.: Geothermal energy systems: exploration, development, and utilization, John Wiley & Sons, 2011.

Hussaini, S. R. and Dvorkin, J.: Specific surface area versus porosity from digital images, J. Pet. Sci. Eng., 196, 107773, 2021.

Ingebritsen, S., Geiger, S., Hurwitz, S., and Driesner, T.: Numerical simulation of magmatic hydrothermal systems, Rev. Geophys., 48, 2010.

Ingebritsen, S. E. and Appold, M.: The physical hydrogeology of ore deposits, Econ. Geol., 107, 559–584, 2012.

Jamtveit, B. and Yardley, B.: Fluid flow and transport in rocks: mechanisms and effects, Springer Science & Business Media, 1996.

- Kaszuba, J., Yardley, B., and Andreani, M.: Experimental perspectives of mineral dissolution and precipitation due to carbon dioxide-water-rock interactions, Rev. Mineral. Geochem., 77, 153–188, 2013.
  - Kelemen, P., Park, A., Matter, J., Gadikota, G., Lisabeth, H., and Zhu, W.: Geo-Chemo-Mechanical Studies for Permanent CO (sub 2) Storage in Geologic Reservoirs, Columbia Univ., New York, NY (United States), 2013.
  - Kelemen, P., Benson, S. M., Pilorgé, H., Psarras, P., and Wilcox, J.: An overview of the status and challenges of CO2 storage in minerals and geological formations, Front. Clim., 1, 9, 2019.
- 1265 Kelemen, P. B., Matter, J., Streit, E. E., Rudge, J. F., Curry, W. B., and Blusztajn, J.: Rates and mechanisms of mineral carbonation in peridotite: natural processes and recipes for enhanced, in situ CO2 capture and storage, Annu. Rev. Earth Planet. Sci., 39, 545–576, 2011.
  - Klimchouk, A., Palmer, A. N., De Waele, J., Auler, A. S., and Audra, P.: Hypogene karst regions and caves of the world, Springer, 2017.
- 1270 Kolditz, O., Shao, H., Wang, W., and Bauer, S.: Thermo-Hydro-Mechanical Chemical Processes in Fractured Porous Media: Modelling and Benchmarking, Springer, 2016.
  - Kouzmanov, K. and Pokrovski, G. S.: Hydrothermal controls on metal distribution in porphyry Cu (-Mo-Au) systems, 2012.
- Ladd, A. J. C. and Szymczak, P.: Use and misuse of large-density asymptotics in the reaction-infiltration instability, Water Resour. Res., 53, 2419–2430, 2017.
  - Lai, P., Moulton, K., and Krevor, S.: Pore-scale heterogeneity in the mineral distribution and reactive surface area of porous rocks, Chem. Geol., 411, 260–273, 2015.
  - Lauwerier, H.: The transport of heat in an oil layer caused by the injection of hot fluid, Appl. Sci. Res. Sect. A, 5, 145–150, 1955.
- 1280 Lichtner, P. C.: The Quasi-Stationary State Approximation to Fluid/Rock Reaction: Local Equilibrium Revisited, in: Diffusion, Atomic Ordering, and Mass Transport: Selected Topics in Geochemistry, edited by: Ganguly, J., Springer US, New York, NY, 452–560, 1991.
  - Lichtner, P. C., Steefel, C. I., and Oelkers, E. H.: Reactive transport in porous media, Walter de Gruyter GmbH & Co KG, 1996.
- 1285 Lighthill, M. J. and Whitham, G. B.: On kinematic waves II. A theory of traffic flow on long crowded roads, Proc. R. Soc. Lond. Ser. Math. Phys. Sci., 229, 317–345, 1955.
  - MacQuarrie, K. T. and Mayer, K. U.: Reactive transport modeling in fractured rock: A state-of-the-science review, Earth-Sci. Rev., 72, 189–227, 2005.
- Maher, K., Steefel, C. I., DePaolo, D. J., and Viani, B. E.: The mineral dissolution rate conundrum: Insights from reactive transport modeling of U isotopes and pore fluid chemistry in marine sediments, Geochim. Cosmochim. Acta, 70, 337–363, 2006.
  - Maliva, R. G.: Anthropogenic aquifer recharge: WSP methods in water resources evaluation series no. 5, Springer, 2019.
- Menzel, M. D., Sieber, M. J., and Godard, M.: From peridotite to listvenite–perspectives on the processes,
  mechanisms and settings of ultramafic mineral carbonation to quartz-magnesite rocks, Earth-Sci. Rev., 104828,
  2024.

- Micklethwaite, S. and Cox, S. F.: Progressive fault triggering and fluid flow in aftershock domains: Examples from mineralized Archaean fault systems, Earth Planet. Sci. Lett., 250, 318–330, 2006.
- Molins, S. and Knabner, P.: Multiscale approaches in reactive transport modeling, Rev. Mineral. Geochem., 85, 27–1300 48, 2019.
  - Mullins, W. W. and Sekerka, R. F.: Morphological stability of a particle growing by diffusion or heat flow, J. Appl. Phys., 34, 323–329, 1963.
  - Noiriel, C.: Resolving Time-dependent Evolution of Pore-Scale Structure, Permeability and Reactivity using {X}-ray Microtomography, Rev Miner. Geochem, 80, 247–285, 2015.
- Noiriel, C., Steefel, C. I., Yang, L., and Ajo-Franklin, J.: Upscaling calcium carbonate precipitation rates from pore to continuum scale, Chem Geol, 318–319, 60–74, 2012.
  - Oliver, N. H. and Bons, P. D.: Mechanisms of fluid flow and fluid—rock interaction in fossil metamorphic hydrothermal systems inferred from vein–wallrock patterns, geometry and microstructure, Geofluids, 1, 137–162, 2001.
- Pacheco, F. A. L. and Aleneoão, A. M. PVan der Weijden, C. H.: Role of fractures in hydraulic diffusivity in the decrease of weathering of solid rocks: narrowing the gap between laboratory and field weathering rates, J. rates over time, J. Hydrol., 316, 248–265, 2006512, 87–106, 2014.
  - Palmer, A. N.: Origin and morphology of limestone caves, Geol. Soc. Am. Bull., 103, 1–21, 1991.
- Pandey, S., Vishal, V., and Chaudhuri, A.: Geothermal reservoir modeling in a coupled thermo-hydro-mechanicalchemical approach: a review, Earth-Sci. Rev., 185, 1157–1169, 2018.
  - Peng, C., Crawshaw, J. P., Maitland, G. C., and Trusler, J. P. M.: Kinetics of calcite dissolution in CO2-saturated water at temperatures between (323 and 373) K and pressures up to 13.8 MPa, Chem Geol, 403, 74–85, 2015.
  - Person, M., Raffensperger, J. P., Ge, S., and Garven, G.: Basin-scale hydrogeologic modeling, Rev. Geophys., 34, 61–87, 1996.
- 1320 Phillips, O. M.: Geological fluid dynamics: sub-surface flow and reactions, Cambridge University Press, 2009.
  - Plummer, L. N., Wigley, T. M. L., and Parkhurst, D. L.: The kinetics of calcite dissolution in CO2-water systems at 5 degrees to 60 degrees C and 0.0 to 1.0 atm CO2, Am. J. Sci., 278, 179-216, https://doi.org/10.2475/ajs.278.2.179, 1978.
- Press, W. H., Teukolsky, S. A., Vetterling, W. T., and Flannery, B. P.: Numerical recipes: The art of scientific computing, Cambridge university press, 2007.
  - Prigiobbe, V., Hänchen, M., Costa, G., Baciocchi, R., and Mazzotti, M.: Analysis of the effect of temperature, pH, CO2 pressure and salinity on the olivine dissolution kinetics, Energy Procedia, 1, 4881–4884, 2009.
  - Rawal, C. and Ghassemi, A.: A reactive thermo-poroelastic analysis of water injection into an enhanced geothermal reservoir, Geothermics, 50, 10–23, 2014.
- 1330 Rimstidt, J. D.: Diffusion control of quartz and forsterite dissolution rates, Appl. Geochem., 61, 99–108, 2015.
  - Rimstidt, J. D. and Barnes, H.: The kinetics of silica-water reactions, Geochim. Cosmochim. Acta, 44, 1683–1699, 1980.

- Rimstidt, J. D., Brantley, S. L., and Olsen, A. A.: Systematic review of forsterite dissolution rate data, Geochim. Cosmochim. Acta, 99, 159–178, 2012.
- 1335 Robb, L.: Introduction to ore-forming processes, John Wiley & Sons, 2005.
  - Roded, R. and Dalton, L. E.: Stability of two-phase flow with interfacial flux in porous media: CO2 mineralization, Phys. Fluids, 36, 2024.
  - Roded, R., Shalev, E., and Katoshevski, D.: Basal heat-flow and hydrothermal regime at the Golan-Ajloun hydrological basins, J. Hydrol., 476, 200–211, 2013.
- 1340 Roded, R., Aharonov, E., Holtzman, R., and Szymczak, P.: Reactive flow and homogenization in anisotropic media, Water Resour. Res., p.e2020WR027518., 2020.
  - Roded, R., Szymczak, P., and Holtzman, R.: Wormholing in anisotropic media: Pore-scale effect on large-scale patterns, Geophys. Res. Lett., e2021GL093659, 2021.
- Roded, R., Aharonov, E., Frumkin, A., Weber, N., Lazar, B., and Szymczak, P.: Cooling of hydrothermal fluids rich in carbon dioxide can create large karst cave systems in carbonate rocks, Commun. Earth Environ., 4, 465, https://doi.org/10.1038/s43247-023-01082-z, 2023.
  - Roded, R., Langford, B., Aharonov, E., Szymczak, P., Ullman, M., Yaaran, S., Lazar, B., and Frumkin, A.: Hypogene speleogenesis in carbonates by cooling hydrothermal flow: The case of Mt. Berenike caves, Israel, Int. J. Speleol., 53, 8, 2024a.
- 1350 Roded, R., Aharonov, E., Szymczak, P., Veveakis, M., Lazar, B., and Dalton, L. E.: Solutions and case studies for thermally driven reactive transport and porosity evolution in geothermal systems (reactive Lauwerier problem), Hydrol. Earth Syst. Sci., 28, 4559–4576, 2024b.
  - Scott, S. W. and Driesner, T.: Permeability changes resulting from quartz precipitation and dissolution around upper crustal intrusions, Geofluids, 2018, 6957306, 2018.
- 1355 Seigneur, N., Mayer, K. U., and Steefel, C. I.: Reactive transport in evolving porous media, Rev. Mineral. Geochem., 85, 197–238, 2019.
  - Sibson, R., Moore, J. M. M., and Rankin, A.: Seismic pumping—a hydrothermal fluid transport mechanism, J. Geol. Soc., 131, 653–659, 1975.
  - Solow, R. M.: A contribution to the theory of economic growth, Q. J. Econ., 70, 65-94, 1956.

1365

- 1360 Stauffer, F., Bayer, P., Blum, P., Molina-Giraldo, N., and Kinzelbach, W.: Thermal use of shallow groundwater, 2014.
  - Steefel, C. and Lichtner, P.: Multicomponent reactive transport in discrete fractures: II: Infiltration of hyperalkaline groundwater at Maqarin, Jordan, a natural analogue site, J. Hydrol., 209, 200–224, 1998.
  - Steefel, C. I. and Maher, K.: Fluid-Rock Interaction: A Reactive Transport Approach, Rev. Mineral. Geochem., 70, 485–532, https://doi.org/10.2138/rmg.2009.70.11, 2009.
  - Szymczak, P. and Ladd, A. J. C.: Reactive-infiltration instabilities in rocks. Fracture dissolution, J. Fluid Mech., 702, 239–264, 2012.
  - Taron, J. and Elsworth, D.: Thermal-hydrologic-mechanical-chemical processes in the evolution of engineered geothermal reservoirs, Int. J. Rock Mech. Min. Sci., 46, 855–864, 2009.

1370 Tripp, G. I. and Vearncombe, J. R.: Fault/fracture density and mineralization: a contouring method for targeting in gold exploration, J. Struct. Geol., 26, 1087–1108, 2004.

Turcotte, D. L. and Schubert, G.: Geodynamics, 3rd ed., Cambridge university press, 2002 New York, 2014.

Vallis, G. K.: Atmospheric and oceanic fluid dynamics, Cambridge University Press, 2017.

Wood, J. and Hewett, T.: Fluid convection and mass transfer in porous sandstones—A theoretical model, Geochim. Cosmochim. Acta, 46, 1707–1713, 1982.

Woods, A. W.: Flow in porous rocks, Cambridge University Press, 2015.

380

375